Mineralogy and Petrology
https://doi.org/10.1007/s00710-024-00850-9

RESEARCH

Deciphering magmatic processes from plagioclase, clinopyroxene and amphibole chemistry and textures: A case study of a basaltic lava flow in the Basque-Cantabrian Basin (Northern Spain)

Alfonso Pesquera[1] · **Pedro P. Gil-Crespo**[1]

Received: 2 October 2023 / Accepted: 24 January 2024

Abstract
This paper addresses the study of a pillow lava interbedded with Late Albian-Early Cenomanian sediments that crops out in Armintza (Bizkaia, Northern Spain). The lava flow is an alkaline basalt with abundant macrocrysts of clinopyroxene, kaersutite, Ca-rich plagioclase (50-86% An) and ilmenite, which display a variety of textures and complex zoning patterns indicative of open-system magmatic behaviour. Macrocryst cores are likely to be inherited antecrysts that underwent complex processes under deep pre-eruptive conditions (≈ 700-800 MPa). Microcrysts and macrocryst rims formed during magmatic ascent and emplacement at shallower levels (≈ 35 MPa). Hypothetical melts in equilibrium with clinopyroxenes and amphiboles have trace element compositions like metasomatic vein melts containing amphibole, and their patterns overlap with those of the Armintza pillow lava. This suggests a metasomatised lithospheric mantle with amphibole-rich veins as a potential source for the alkaline basaltic melt. It is even conceivable that the Armintza pillow lava and other alkaline volcanic manifestations of the Basque-Cantabrian Basin were part of the same magma plumbing system through which a series of time-limited eruptions of different batches of magma ascended from the lithospheric mantle to the upper crust during the Albian to the Santonian.

Keywords Basaltic pillow-lava · Mineral textures and composition · Alkaline magmatism · Basque-Cantabrian Basin

Introduction

Petrographic studies of igneous rocks reveal a wide range of mineral textures as a result of the diverse history of magmatic systems. Minerals often preserve valuable information about the plumbing systems and processes that magma undergoes through the crust from the earliest stages of crystallization. In volcanic environments, phases such as plagioclase, olivine, pyroxene, amphiboles and other minerals have often been used to shed light the pre-eruptive history and evolution of magmas (e.g., Streck 2008; and references therein;). The study of crystal populations within an igneous rock, and the textural relationships between them, are of paramount importance to understand the magmatic systems, the magma storage depths and the characteristics of the main magmatic stages from the source to the last episodes of its evolution (Jerram et al. 2018; and references therein). Several populations of crystals in a magma denote changing magmatic conditions and varying degrees of undercooling that give rise to various nucleation and growth events. Undercooling-driven variations and crystallization kinetics dictate the textural evolution of magmas, crystal shape and zoning, the degree of compositional heterogeneity within crystals and element partitioning. At low undercoolings, growth dominates nucleation producing euhedral planar-faceted crystals, while at high undercoolings nucleation dominates growth promoting the formation of numerous small crystals with disequilibrium morphologies (e.g., Watanabe and Kitamura 1992; Mollo and Hammer 2017, and references therein; Giuliani et al. 2020). Crystallization of plagioclase, pyroxene and amphibole with a variety of textures and compositions induced by changes in physical and chemical variables is very common in mafic magmas. However, all phases must be considered for a correct interpretation on the undercooling mechanism and crystallization kinetics, although many of the differences are subtle and difficult to establish (Shea

Editorial handling: C. Wang

✉ Alfonso Pesquera
alfonso.pesquera@ehu.eus

[1] Department of Geology, University of the Basque Country (UPV/EHU), Barrio Sarriena s/n, 48940 Leioa, Bizkaia, Spain

Published online: 13 May 2024

and Hammer 2013). Despite this, plagioclase, pyroxene and amphibole are excellent forensic minerals to elucidate the conditions of the magma storage zone and its evolution. Hence these minerals have attracted considerable attention and spawned long-lasting discussion among many researchers. (e.g., Streck 2008, and references therein; Viccaro et al. 2010; Shane and Smith 2013; Erdmann et al. 2014; Coote and Shane 2018; Ubide and Kamber 2018; Bennett et al. 2019; Kamaci and Altunkaynak 2019; van Gerve et al. 2020; Cao et al. 2022; Molendijk et al. 2022). In addition, the depth and conditions of magma storage influence the eruptive style, which may be useful to distinguish between end-member models, ranging from mush-dominated magmas throughout the bulk-crust and liquid-rich magmas circumscribed to discrete storage reservoirs (e.g. Cashman et al. 2017; Edmons et al. 2019; Sparks et al. 2019).

Several outcrops of volcanic rocks occur in the Basque-Cantabrian Basin as a result of the Mesozoic magmatic activity around the North Atlantic, which is characterised by the following features: (1) tholeiitic sequences of Triassic-Liassic age and Cretaceous sequences of alkaline affinity; and (2) distribution along regional lineaments, which have been interpreted as hot-spot traces on the American margin or as a consequence of crustal extension and thinning in the Pyrenees during the opening of the Atlantic Ocean (Azambre et al. 1992). The Cretaceous alkaline sequences occur mainly in three areas, Corbières, Central Pyrenees and the Basque-Cantabrian Basin (Fig. 1), including basaltic lavas, mafic to ultramafic intrusive rocks and feldspathoidal syenites (Azambre et al. 1992; Castañares et al. 1997; Ubide-Garralda 2013; Sarrionandia-Eguidazu et al. 2017).

In this paper, we address the study of a basaltic pillow-lava interbedded with Late Albian-Early Cenomanian sediments outcropping in Armintza (Bizkaia), which was emplaced during the submarine volcanism associated with the Cretaceous magmatism of the Basque-Cantabrian Basin. The volcanic rock is characterised by showing a large number of macrocrysts scattered throughout the lava in an aphanitic groundmass. We attempt to elucidate the history of the pillow-lava using the textural and compositional record preserved in plagioclase, pyroxene and amphibole macrocrysts. Our work on the pillow-lava of Armintza integrates a

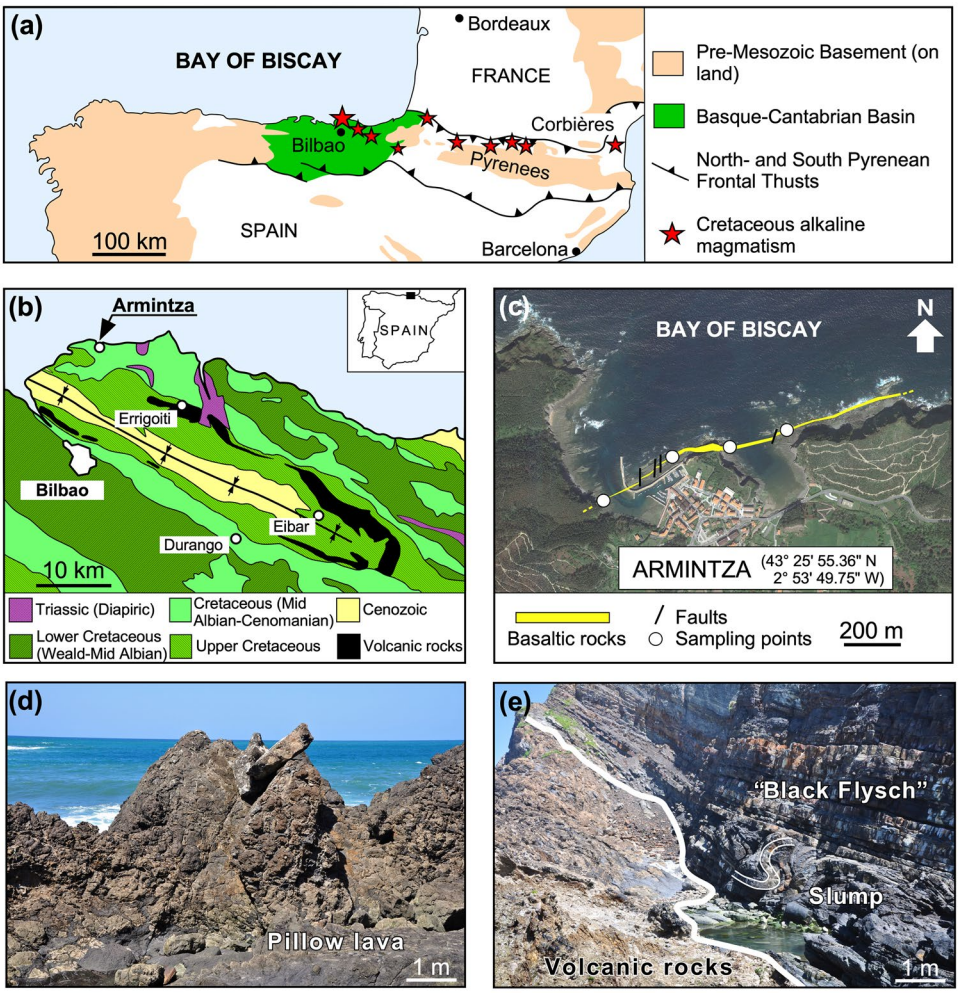

Fig. 1 **a** Regional setting of the Cretaceous alkaline magmatism (modified of Castañares et al. 2001). **b** Simplified geological map and distribution of volcanic rocks in the Biscay synclinorium. **c** Exposition of the basaltic lava flow at Armintza. **d** Pillow-lava lobes **e** Contact of the pillow lava with the flysch. Note the slump folds between the volcanic rock and the sedimentary sequence. The folding is interpreted to be syn-depositional by the undisturbed character of the bedding above

detailed petrographic study, bulk rock and mineral chemistry in an effort to unravel the pre-eruptive magmatic conditions, the magma source, as well as their significance in a regional context. As a result of it, we propose an open-system processes during magma evolution and a metasomatised lithospheric mantle as the most probable source of the alkaline basaltic melt.

Geological setting

The Basque-Cantabrian basin forms part of the Bay of Biscay-Pyrenean domain. It is considered to be a segment of the Pyrenean system that connects the Pyrenees and the Cantabrian mountains and marks the dividing line between the Iberian Peninsula and continental Europe (Fig. 1a). The formation of this basin is the result of a sequence of geological process that occurred during the pericratonic rift related to opening of the Bay of Biscay-Pyrenean rift system (see Robles 2014, for an overview on the geological evolution of this basin). The rifting provoked a lithosphere thinning and in the Basque-Cantabrian Basin was controlled by an extensional detachment active between Valanginian and early Cenomanian times. There is a broad consensus that the Basque-Cantabrian Basin opened by transtensional stretching of the lithosphere in relation with oblique rifting, and subsequently inverted during the Pyrenean orogeny. Nevertheless, significant discrepancies exist regarding the kinematic model for the opening and tectonic inversion of the Basque-Cantabrian Basin (Miró et al. 2021, Pedrera et al. 2021, and references therein). During the Cretaceous, sedimentary processes gave rise to several syn-rift and post-rift depositional sequences. A two-sided basin in a deep trough between the Iberian and European plates developed, with high subsidence rates and great accumulation of sediments because of the hyperextension and counterclockwise rotation of the Iberian plate. This basin is characterised by a thick siliciclastic or calcareous turbidite sequence and pelagic deposits formed from Albian to the early Eocene. The opening period ended with the convergence between the Iberian and Eurasian plates that inverted the Cantabrian-Pyrenean rift system and led to the formation of synorogenic deposits (see Robles 2014, for further details).

Based on gravity data, Pedrera et al. (2017) postulated that the mantle reached relatively shallow crustal levels along the Biscay synclinorium, close to the north basin boundary. The asthenosphere ascent promoted partial melting of the lithospheric mantle during rifting, with stretching-driven melt percolation as a result of lithospheric-scale deformation (Pedrera et al. 2021). The magmatism of the Basque-Cantabrian Basin includes two main syn- and post-rift magmatic events that took place between the Triassic and the Late Cretaceous. Leaving aside the tholeiitic diabases that are widespread within the Upper Triassic salt levels, the Cretaceous magmatism of the Basque Cantabrian Basin is of alkaline characteristics and spans from the Valanginian to Santonian (Lamolda et al. 1983; García-Garmilla and Carracedo-Sánchez 1989; Montigny et al. 1986; García-Mondejar et al. 2018). The magmatic locus was located along the rift axis in this period, with magmatic flow peaking during extensional deformation and late stages of rifting (Ubide et al. 2014a; Pedrera et al. 2021). In particular, it is noteworthy that the intermittent submarine volcanism occurred coeval with marine sedimentation during the Albian to the Santonian (Castañares and Robles 2004; Carracedo-Sánchez et al. 2012). This volcanism forms part of the Cretaceous alkaline magmatism from the North-Pyrenean Rift zone (Fig. 1a), and in the Basque-Cantabrian Basin is mainly represented by basalts with minor amounts of trachyte to trachyandesite that occur along the Alpine Biscay synclinorium as a thick sequence (> 1.000 m thick) interbedded with Cretaceous sediments (Fig. 1b). The volcanic sequence shows characteristics typical of eruptions under shallow submarine conditions including sheet flows of massive to columnar aspect, pillow lavas, pillow breccias, and a wide range of volcaniclastic (hyaloclastite, autobreccia, peperite, and talus debris) deposits, as well as syn-eruptive reworked facies (Castañares et al. 1997; Carracedo et al. 1999).

The studied basaltic lava flow is located in Armintza, a little town of the Bay of Biscay (Spain), and represents a relatively early (Albian) manifestation of the submarine volcanism in the Basque-Cantabrian Basin. It extends superficially ≈ 1100 m with a direction N50-N70°E, plunging into the sea towards the SE with a variable dip and thickness, 40-60°SE and 2-15 m, respectively (Fig. 1c). The basaltic lava shows a pillow structure (Fig. 1d) and is interbedded concordantly with sediments from the western Pyrenees Black Flysch of the late Albian-Lower Cenomanian. The base of the flow is roughly flat but in detail intermingled contacts between lava and sediment can be observed. The upper contact is characterised by the presence of slump folds in the turbidite sequence (Fig. 1e).

Analytical methods

Bulk-rock composition

Rock sampling has been carried out at four different points along the lava, in principle without obvious alteration (Fig. 1c). A petrographic study has been carried out on twenty-one samples from cross sections corresponding to the four different sampling points. Relative amounts of macrocrysts of three representative rock samples were estimated following the procedure for porphyritic rocks described in Hutchison (1974). Bulk-rock composition was determined

by crushing rock samples (about 3.0 kg per sample) down to a final particle size of < 1mm with a jaw crusher. Subsequently, the samples were pulverized with a ring mill and reduced by the method of coning and quartering, taking the two diagonally opposite quarters for chemical analysis. Major elements were determined at the Granada University by X-ray fluorescence (XRF) on fused glass discs using a Philips PW1404/10 X-ray spectrometer. Zr was also analysed by X-ray fluorescence using pellets of pressed rock powder. X-ray counts were translated into concentrations by a computer program based on De Jongh (1973) fundamental parameter method. Calibration curves were based on international rock standards (Govindaraju 1994), and the BHVO, BR and GSR3 standards were used as control samples. Precision was of 2–5% for major elements, except Mn and P (5–10%), and 2–5% for Zr. Trace elements were analysed by ICP-MS (NexION 300D Quadrupole Ion Filter Plasma Torch Ionization Source Mass Spectrometer), after HNO_3 + HF digestion of 100 mg of sample powder in a Teflon-lined vessel at 180 ºC and 200 p.s.i. for 30 min, evaporation to dryness and subsequent dissolution in 100 ml of 4 vol% HNO_3. Precision is better than ±5% for analyte concentrations of 10ppm.

Mineral composition

Major elements of plagioclase (n = 220), pyroxene (n = 280), amphibole (n = 140), rhönite (n = 40), ilmenite (n = 25), apatite (n = 10) and pyrrhotite (n = 5) were determined at the University of Oviedo using a CAMECA SX100 electron microprobe, equipped with four wavelength-dispersive spectrometers. The operating conditions were an accelerating voltage of 15 kV with a beam current of 30nA and a 2 µm focussed electron beam. The calibration standards used were natural orthoclase for K, natural wollastonite for Ca, synthetic $MnTiO_3$ for Mn and Ti, natural magnetite for Fe, natural albite for Na, synthetic Cr_2O_3 for Cr, synthetic Al_2O_3 for Al, natural forsterite for Mg, natural apatite for P, IR-X for Rb, LiF for F and vanadinite for Cl. Data were reduced using the procedure of Pouchou and Pichoir (1985). Analytical errors are estimated to be of the order of ±1–2% for major elements and ±10% for minor elements. Backscatter electron (BSE) images of pyroxene grains were taken by using a CAMECA SX100 electron microprobe (University of Oviedo). Data were collected at 15 kV and 40 nA beam current, with an analytical step size of 1 µm.

The calculation of the amphibole formula was carried out on the basis of 24(O, OH, F, Cl) with (OH, F, Cl) = 2 apfu (Hawthorne et al. 2012), and the Fe^{3+} content has been estimated using the relation between Fe^{3+} and (OH+F): Fe^{3+} = (1.16 - OH - F)/1.01 (Popp et al. 2006). Analyses of pyroxenes and plagioclases have been recalculated on the basis of 6 oxygens and 32 oxygens according to Morimoto et al. (1988) and Deer et al. (2013), respectively. Fe^{3+} in pyroxenes has been estimated adjusting Fe^{3+}/ Fe_{tot} ratio for electroneutrality. We calculated the rhönite formula using stoichiometry, and the Fe^{3+}/Fetot ratio was estimated assuming 40 oxygens and 28 cations (Grew et al. 2008).

Trace elements analyses of pyroxene and amphibole were performed by LA-ICP-MS at the University of Granada using a 213 nm Mercantek Nd-YAG laser coupled to a NexION 2000b Quadrupole Ion Filter Plasma Torch Ionization Source Mass Spectrometer, with a shielded plasma torch, and the NIST-610 glass as external standard. The ablation was carried out in a He atmosphere. The laser beam was fixed at 60-95 µm diameter. The spot was pre-ablated for 45 seconds using a laser repetition rate of 10 Hz and 40% output energy. Then the spot was ablated for 60 seconds at 10 Hz with a laser output energy of 75%. In order to minimize mass fractionation and to increase sensitivity the sample stage was set to move upwards 5 mm every 20 seconds. In each analytical session of a single thick section (100 µm), the NIST-610 glass was analysed at the beginning and at the end, and also after every nine spots to correct for drift. Geostandars used were the PMS, WSE, UBN, BR and AGV (Govindaraju 1994). Concentration values were corrected using silicon as an internal standard. Data reduction was carried out with a custom software (freeware available from F. Bea) of the STATA commercial package. The precision, calculated on five to seven replicates of the NIST-610 glass measured in every session, was in the range ± 3 to ± 7% for most elements.

Mössbauer spectroscopy

In order to estimate the amount of Fe^{3+} in pyroxene and amphibole, mineral separates from three rock samples were prepared by breaking up them into smaller chips, then sieved for sizing, and hand picking the small crystal fragments under a binocular microscope for analysis by Mössbauer spectroscopy at the Basque Country University (Department of Electricity and Electronics). ^{57}Fe-Mo Mössbauer spectra were acquired at room temperature using a standard spectrometer with a Co/Rh source. The isomer shift is reported relative to metallic iron. All the spectra were collected in a multi-channel analyser with 512 channels, and the experimental data were evaluated by means of a least-squares fitting.

General petrography and bulk-rock chemistry

The pillow lava of Armintza is a porphyritic aphanitic basalt containing macrocrysts (up to 5 cm, mostly < 1.5 cm) and spherical vesicles (generally < 2 mm in diameter) unevenly distributed throughout the rock. The total macrocrysts abundance is high, from ≈ 25 to 50 vol%. Large macrocrysts and microphenocrysts (≈ 200-1000 µm) comprise plagioclase

(5-15 vol%), clinopyroxene (9-25 vol%), amphibole (3-16 vol%) and ilmenite (2-6 vol%). Apatite and pyrite microphenocrysts occur in minor quantities, and the vesicles represent < 5vol%. A common feature is the occurrence of glomerocrysts and clusters of macrocrysts involving plagioclase ± pyroxene ± amphibole ± ilmenite. The very fine-grained groundmass has an intersertal texture and includes an interlocking network of tabular to spiky plagioclase microlites, as well as abundant more equant-shaped grains of pyroxene, rhönite closely linked to amphibole macrocrysts, apatite, ilmenite and pyrite ± pyrrhotite. Vesicles (generally ≤ 5 vol%) are mainly filled by calcite and minor chlorite. The macrocrysts/groundmass ratio tends to be lower in contact zones than in internal zones. Although the pillow lava presents a variable alteration, especially on the contact zones of the pillow lava, the plagioclase, pyroxene and amphibole macrocrysts are relatively well preserved in most samples of internal zones.

Regarding the bulk-rock chemistry of the Armintza pillow lava, the following characteristics should be noted: (1) Chemical composition typical of alkaline basalts without significant variations throughout the lava, with 42.3-42.6 wt% SiO_2, 14.87-14.92 wt% Al_2O_3, 4.35-4.42 wt% TiO_2, 10.3-11.5 wt% FeO, 7.3-7.6 wt% MgO, 11.9-12.3 wt% CaO and 2.4-2.5 wt% Na_2O (Table 1). (2) Enrichment of incompatible trace elements compared to mid-ocean ridge basalts (MORB), both N-Type and E-type (Fig. 2a). (3) REE contents as well as Al_2O_3/TiO_2 (3.38-3.41), Na_2O/K_2O (2.6-3.5), Th/Yb (2.6-2.7), Nb/Yb (43.5-45.5) and TiO_2/Yb (2.5-2.6) ratios are typical of volcanic alkaline rocks with OIB affinities (Fig. 2a, b, c, d, e). Low Zr/Nb (2.34-2.48) ratios are also consonant with this type of rocks. εNd(t) values recorded for alkaline basalts from the Basque-Cantabrian basin are consistent with OIB sources, and similar to those found in extension and rift settings (Rossy et al. 1992).

Mineral textures and composition

Plagioclase

Plagioclase occurs as macrocrysts (mostly ≤ 1.0 cm) and microlites (mostly ≤ 150 µm) exhibiting tabular to skeletal,

Table 1 Major and trace elements compositions for the Armintza basaltic lava

Sample	PT-04-7	PT-04-3	PT-04-4	PT-04-7		PT-04-3	PT-04-4
Major oxides (wt%)				Trace elements (ppm)			
SiO_2	42.34	42.62	42.46	Nb	77.5	74.3	78.5
TiO_2	4.39	4.42	4.35	Sc	26.8	25.6	27.8
Al_2O_3	14.89	14.92	14.87	Y	22.8	22.9	22.9
FeOtot	10.68	10.28	11.53	Ta	5.5	5.3	5.5
MnO	0.11	0.11	0.13	Zr	181.9	177.6	184.3
MgO	7.46	7.58	7.32	Hf	4.7	4.5	4.7
CaO	11.98	11.92	11.59	Mo	2.9	3.0	3.1
Na_2O	2.48	2.42	2.38	Th	4.7	4.5	4.7
K_2O	0.71	0.82	0.92	U	1.2	1.2	1.3
P_2O_5	0.50	0.45	0.45	Pb	2.1	2.8	2.1
LOI	4.38	4.45	4.03	Ga	20.6	19.8	19.4
Total	99.92	99.99	100.03	Tl	0.1	0.1	0.1
Trace elements (ppm)				REE (ppm)			
Cs	1.1	1.2	1.2	La	50.7	49.7	49.7
Rb	14.5	34.0	18.7	Ce	103.4	99.4	100.5
Ba	1127.8	1219.6	1026.7	Pr	12.8	12.4	12.6
Sr	1321.5	1294.2	1234.4	Nd	50.9	50.0	51.0
Li	57.6	29.1	54.7	Sm	9.3	8.9	9.8
Be	0.7	0.8	0.8	Eu	3.1	3.1	3.0
Sn	2.3	2.3	2.3	Gd	7.6	7.5	7.6
Cu	51.2	47.9	47.4	Tb	1.1	1.0	1.0
Zn	120.6	117.0	93.6	Dy	5.4	4.9	4.9
Co	44.9	43.9	43.9	Ho	0.9	0.9	0.9
V	491.7	480.1	483.7	Er	2.1	2.1	2.1
Ni	68.6	76.9	68.6	Tm	0.3	0.3	0.3
Cr	151.7	141.0	154.8	Yb	1.7	1.7	1.7

LOI loss of ignition

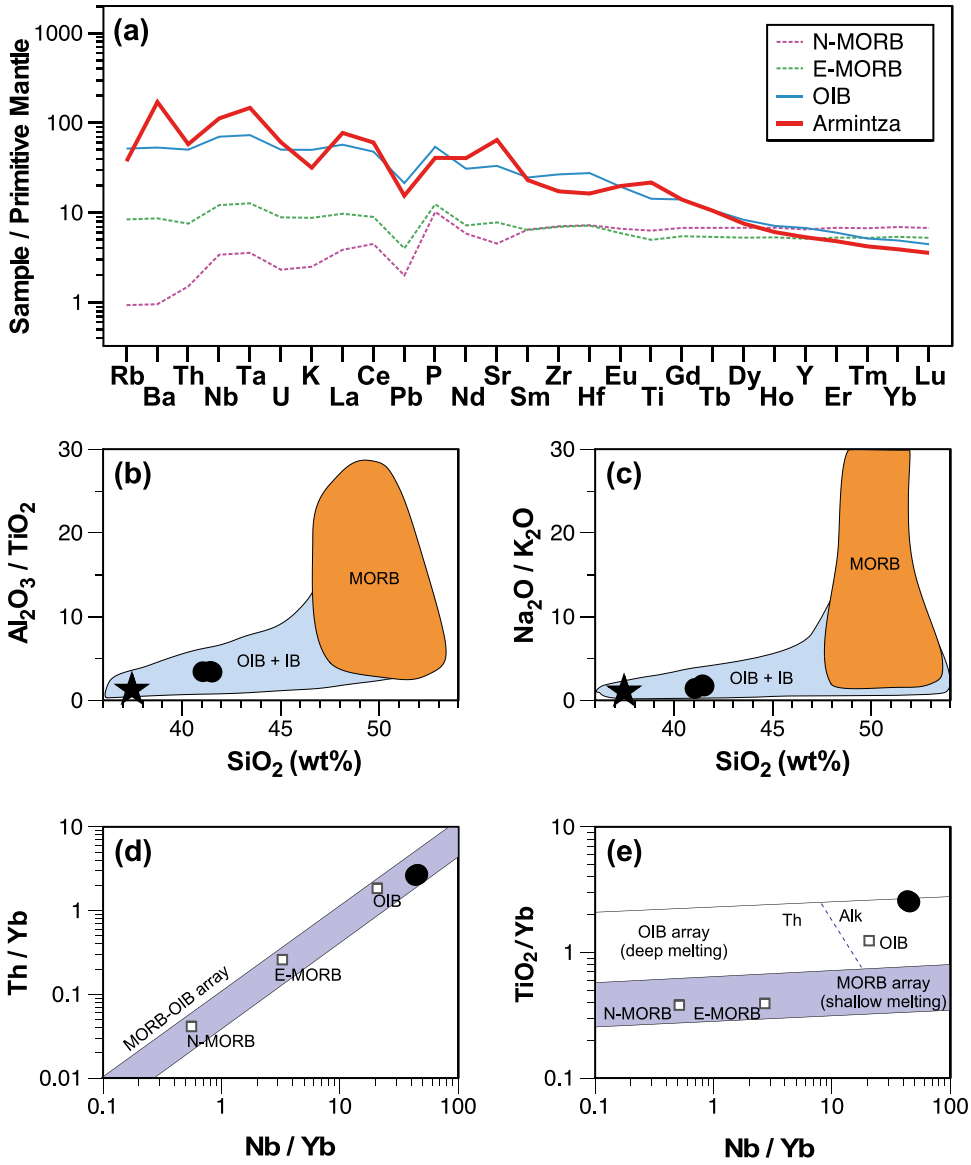

Fig. 2 **a** Trace-element contents of the pillow lava observed in Armintza (normalised to primitive mantle (McDonough and Sun 1995). **b** Al_2O_3/TiO_2 vs. SiO_2 diagram; **c** Na_2O/K_2O vs. SiO_2 diagram (Pilet 2015); **d** Th/Yb vs. Nb/Yb ratio. **e** TiO_2/Yb vs. Nb/Yb ratio (modified of Pearce 2008). OIB: Ocean Island Basalts; IB: Intraplate Basalts. MORB: Mid-Ocean Ridge Basalts. Black circles: Bulk-rock compositions. Stars: Average composition of amphiboles of this study

elongate and swallowtail morphologies. Macrocrysts are common and show a variety of crystal morphologies, from tabular to strongly resorbed habits, with complex zoning patterns and superimposed resorption events that are hard to explain by simple crystallization paths. Plagioclase compositions vary in general within the ranges An50-An86 and An62-An73 for macrocrysts and microlites, respectively. TiO_2, FeO and MgO contents vary in the range 0.03-0.12 wt%, 0.32-0.64 wt% and 0.02-0.11 wt%, respectively (Table 2).

Four main textural types of plagioclase macrocrysts can be recognised, which are commonly juxtaposed in the same thin section. (1) Coarse to fine sieve-textured plagioclase with a tabular to resorbed habit is the most common type (Fig. 3a). Groundmass inclusions are subrounded to amoeboidal in shape and they may be isolated in a random distribution or interconnected. In this case, the inclusions tend to elongate parallel to lamellar twin planes and may cross laterally to interconnect with adjacent ones. An irregular to amoeboid or geometric, patchy zoning is commonly superimposed on the sieve texture and is often associated to groundmass inclusions (Fig. 3a). Sieve-textured plagioclase may show (i) narrow inclusion-free rims (≈ 10-40 μm) of either more sodic or more calcic plagioclase, which may be connected with inner patches; or (ii) dusty mantles (< 100 μm) followed by ≈ 20-60 μm thick, An-rich rims (73-80% An). In this case, a convolute zoning may develop in the sieve-textured core near the dusty zone (Fig. 3b). (2) Subrounded, variably resorbed macrocrysts with relatively clear cores surrounded by a dusty zone, followed by a clear more calcic rim (mostly < 60 mm) (Fig. 3c). The cores are compositionally homogenous but, in some cases a delicate patchy zoning can be observed. Compositional profiles of

Table 2 Selected chemical compositions, calculated mineral formulae and calculated end-member fractions for plagioclase

Sample nº	1	2	3	4	5	6	7	8	9	10	11	12
Zone	Cores						Rims					
Major oxides (wt%)												
SiO_2	46.68	53.52	46.96	55.44	54.14	53.90	49.98	49.04	48.89	49.82	49.07	50.32
TiO_2	0.09	0.05	0.08	0.03	0.06	0.04	0.09	0.07	0.12	0.09	0.10	0.11
Al_2O_3	32.55	28.61	33.42	27.63	27.97	28.66	30.96	31.54	31.54	31.52	30.83	29.93
FeOtot	0.57	0.56	0.48	0.45	0.32	0.47	0.60	0.57	0.56	0.58	0.64	0.63
MnO	0.01	bdl	bdl	0.00	0.02	0.00	0.02	0.04	bdl	0.02	0.03	0.05
MgO	0.06	0.04	0.07	0.06	0.02	0.02	0.08	0.08	0.07	0.08	0.07	0.11
CaO	16.87	11.65	17.64	10.09	11.10	11.15	14.56	15.18	15.79	15.47	14.76	13.30
Na_2O	1.73	4.85	1.59	5.48	5.21	5.02	3.08	2.86	2.45	2.61	2.98	3.07
K_2O	0.20	0.64	0.15	0.83	0.64	0.65	0.39	0.30	0.30	0.34	0.39	0.66
Total	98.76	99.93	100.38	100.00	99.47	99.92	99.75	99.69	99.72	100.53	98.87	98.18
Calculated mineral formulae (apfu)*												
Si	8.709	9.740	8.628	10.028	9.872	9.789	9.175	9.028	9.003	9.085	9.107	9.356
Al	7.160	6.139	7.238	5.892	6.013	6.136	6.701	6.845	6.846	6.777	6.745	6.561
Ti	0.013	0.007	0.012	0.004	0.008	0.006	0.012	0.010	0.016	0.012	0.014	0.015
Fe^{2+}	0.089	0.085	0.074	0.068	0.049	0.072	0.092	0.088	0.087	0.088	0.100	0.099
Mn	0.001	-	-	0.000	0.002	0.000	0.004	0.006	-	0.004	0.005	0.009
Mg	0.015	0.010	0.018	0.017	0.005	0.005	0.021	0.021	0.019	0.023	0.020	0.029
Ca	3.373	2.271	3.473	1.956	2.168	2.170	2.864	2.995	3.115	3.023	2.935	2.649
Na	0.627	1.712	0.565	1.921	1.842	1.769	1.096	1.022	0.875	0.923	1.071	1.107
K	0.048	0.149	0.034	0.192	0.150	0.151	0.092	0.071	0.071	0.080	0.093	0.157
Calculated end-member fractions (mol%)												
An	0.83	0.55	0.85	0.481	0.521	0.531	0.71	0.73	0.77	0.75	0.716	0.677
Ab	0.15	0.41	0.14	0.472	0.443	0.432	0.27	0.25	0.22	0.23	0.261	0.283
Or	0.01	0.04	0.01	0.047	0.036	0.037	0.02	0.02	0.02	0.02	0.023	0.040

* Calculated based on 32 O atoms per formula unit

FeOtot FeO total, *bdl* below detection limit

this type of plagioclases are characterised by relatively low-An cores with small variations in An (< 5% An), and substantial increase in the An content (up to ≈ 20% An) through the dusty zones with An-rich rims (Fig. 3d). FeO, TiO_2 and MgO contents show similar trends across the plagioclase profiles with higher values in the rim zones (Fig. 3d). The compositional change (ΔXi) across the dusty zone is defined as $Xi_{inboard}$ - $Xi_{outboard}$, with values of ΔAn = -3 to -22%, ΔFeO = -0.02 to -0.16, ΔTiO_2 = -0.01 to -0.11, and ΔMgO = -0.00 to -0.08. (3) Clear plagioclase or containing few inclusions that present a tabular habit and partial resorption in some cases. This type is less common in large macrocrysts than in microphenocrysts. In fact, the latter are the only ones that can appear completely free of inclusions. The crystals commonly exhibit a subrounded core, unzoned or with patchy to spongy-cellular texture, which is encapsulated by a mantle with irregular oscillatory zoning and a more calcic or sodic narrow rim (< 50 µm) (Fig. 3e, f). The compositional oscillations, however, could not be expressed by a periodic variation but rather the result of pulses of growth alternating with periods of dissolution, as suggested by Pearce and Kolisnik (1990). (4) Subhedral to anhedral crystals of dusty plagioclase, which occur as: (i) plagioclase crystals with a completely dusty inner zone surrounded by a An-rich rim (74-82% An) (Fig. 3g), and to a lesser extent (ii) completely dusty crystals.

Plagioclase glomerocrysts show characteristic features of crystallization in crystal-rich environments (Holness et al. 2019). They consist of aggregates of randomly oriented plagioclase crystals, with embedded contacts and irregular grain boundaries derived from the impingement of grains, which are cemented by groundmass material (Fig. 3h).

Clinopyroxene

Clinopyroxene macrocrysts show a variable grain size and the largest macrocrysts may reach up to 5 cm in length. They have a prismatic euhedral to anhedral habit, with pinkish brown, pale brown, yellowish green to pale green colours in thin section, and the crystals commonly exhibit complex

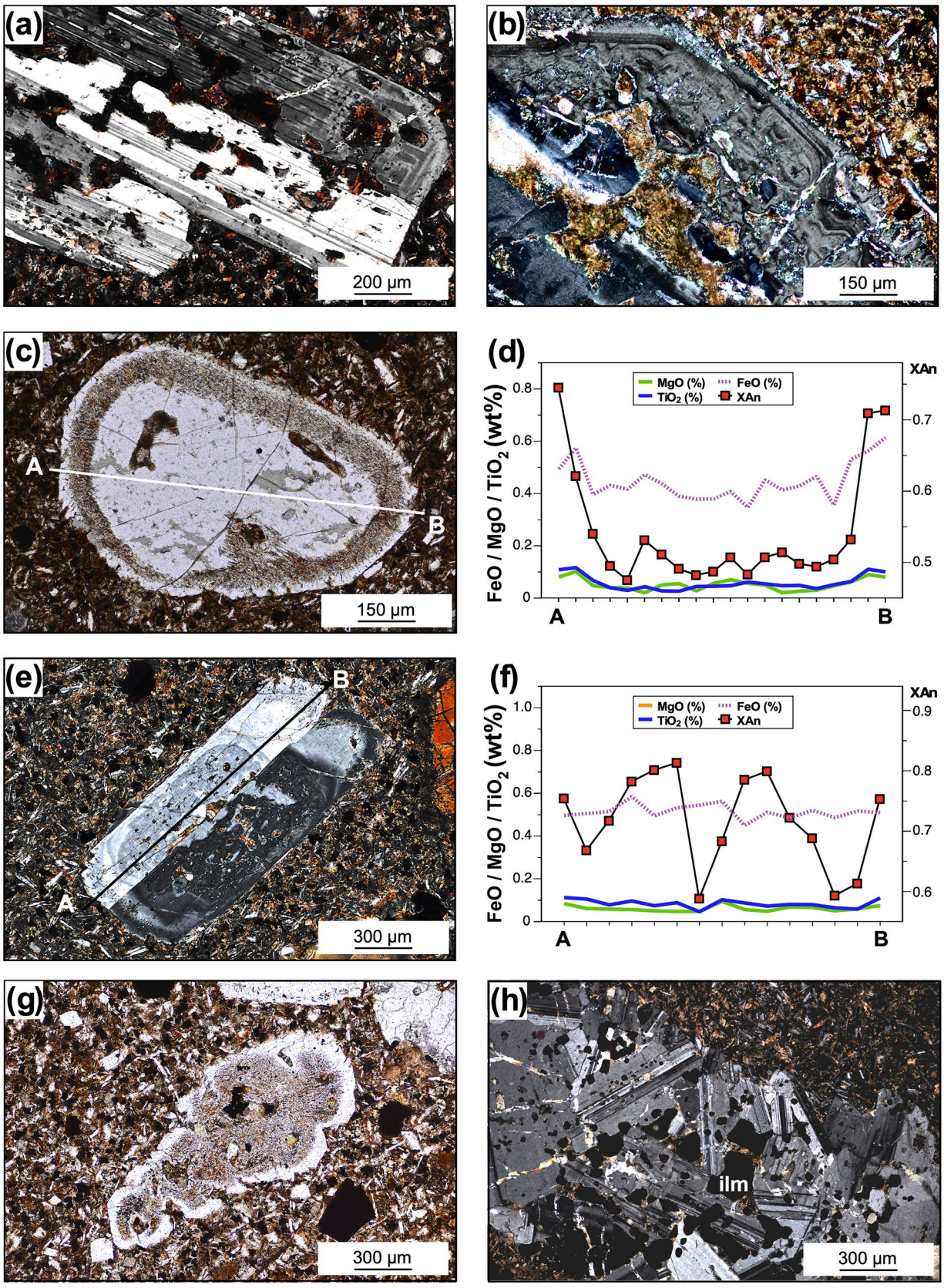
(a)
200 μm
(b)
150 μm
(c)
A
B
150 μm
(d)
MgO (%)
FeO (%)
TiO2 (%)
XAn
FeO / MgO / TiO2 (wt%)
XAn
0
0.2
0.4
0.6
0.8
0.5
0.6
0.7
A
B
(e)
B
A
300 μm
(f)
MgO (%)
FeO (%)
TiO2 (%)
XAn
FeO / MgO / TiO2 (wt%)
XAn
0
0.2
0.4
0.6
0.8
1.0
0.6
0.7
0.8
0.9
A
B
(g)
300 μm
(h)
ilm
300 μm

◂**Fig. 3** **a** Coarse sieve-textured plagioclase displaying patchy zoning (74-79% An) and oscillatory zoning in the rim (80-83% An); **b** Coarse sieve-textured plagioclase core followed by a mantle with convolute zoning and then a dusty zone surrounded by a thin clear rim (70-72% An); **c** Subrounded clear plagioclase core with a dusty zone surrounded by a thin An-rich rim; **d** Intracrystal compositional variation corresponding to the plagioclase of **c**. **e** Plagioclase showing a core with cellular texture, followed by a mantle with complex zoning including diffuse high frequency oscillations, resorption surfaces and superimposed low amplitude oscillations with a thin calcic rim (75-77% An). **f** Intracrystal compositional variation corresponding to the plagioclase of **e**. **g** Dusty plagioclase armoured by a resorbed thin clear rim (74% An). **h** Monomineralic glomerocryst of plagioclase with plagioclase crystals at low to high angles to one another (ilm: ilmenite)

compositional zoning patterns. Inclusions of ilmenite ± pyrite ± apatite are commonly observed. Like plagioclase, many clinopyroxene macrocrysts display external and/or internal resorption features and can be grouped into four major types from textural and compositional point of view. (1) Euhedral macrocrysts consist of light brown euhedral to rounded cores, relatively homogeneous or showing minor compositional variations, which are encapsulated by clear or dusty pinkish-brown rims (mostly 10-80 µm thick) with sector zoning ± fine-scale oscillatory zoning (Fig. 4a, b, c, d). Mg and Ti show symmetrical compositional patterns, and the rims may be richer or poorer in Mg than cores. Sector zoning in rims seems to be due to differential partitioning of Mg, Ti and Al amongst prism sectors (see Fig. S1 in electronic supplementary material). (2) Euhedral to subhedral macrocrysts with concentric, oscillatory zoning towards the rim, which may include a more or less resorbed greenish core (Fig. 4e). This type of pyroxenes is characterised by Mg-poor and Al-Ti rich cores (Fig. 4f). (3) Euhedral macrocrysts that include a core with intricate zoning, a mantle showing oscillatory zoning of variable wavelength, and a rim with sector zoning (Fig. 4g, h). (4) Anhedral to subhedral macrocrysts showing strong external and internal resorption, commonly with ragged rims and in some cases displaying partial shells with radial fibrous texture (Fig. 4i, j, k). (5) Pyroxene macrocrysts that consist of cores pseudomorphed by a brown crystal patchwork and euhedral to subhedral overgrowths (Fig. 4l).

Representative analyses of pyroxene are listed in Table 3. Clinopyroxene macrocrysts and microphenocrysts span a relatively narrow compositional range, corresponding to ternary compositions: $Wo_{47-52}En_{32-42}Fs_{11-20}$. They are considered mostly as subsilicic titanian ferrian diopside following the criteria of Morimoto et al. (1988), with 3.0-12.1 wt% (avg. 8.89 ± 1.84) Al_2O_3, 1-6 wt% (avg. 3.41 ± 0.92) TiO_2, 5.60-9.35 wt% (avg. 7.44 ± 1.31) FeO, 9.47-13.98 wt% (avg. 11.91 ± 1.05) MgO, 20.36-23.02 wt% (avg. 22.17 ± 0.48) CaO and 0.40-0.80 wt% (avg. 0.55 ± 0.10) Na_2O. The Fe^{3+}/Fetot ratio inferred from Mössbauer spectroscopy of three samples is ≈ 0.40. Cr concentrations vary at crystal scale, from contents below the detection limit to relatively high in Cr_2O_3 (up to 0.50 wt%). Clinopyroxene macrocryst compositions are characterised by Mg# values ranging from 61 to 83, where Mg# = 100MgO/(MgO+FeO) on a molar basis, with considerable variability in TiO_2, SiO_2 and Al_2O_3 (Fig. 5a, b, c, e). The rims mostly have higher Ti/Al than cores and some pyroxenes show cores relatively rich in Cr (Fig. 5d, f). Furthermore, there are no clear compositional trends accounting for a simple liquid line of descent of a basaltic liquid (Fig. 5). There are also no significant differences between pyroxenes of the groundmass and the rims of macrocrysts. As a whole, clinopyroxene compositions are typical of alkaline magmas according to Le Bas (1962) and are consistent with pyroxenes from intraplate alkaline basalts using the discriminant function diagram of Nisbet and Pearce (1977). In addition, the studied clinopyroxenes have higher TiO_2, Al_2O_3 and FeO, but lower SiO_2, Cr_2O_3, MgO and Na_2O contents than magmatic pyroxenite veins and peridotite xenoliths (Witt-Eickschen et al. 2003; Powell et al. 2004). Primitive mantle-normalised trace-elements patterns for clinopyroxenes are characterised by a low concentration of large ion lithophile elements (LILE), enrichment of LREE relative to HREE with a general concave-downward REE pattern, positive (Ti, Ta) and negative (Zr, Nb) anomalies. The transitions elements (TE) present troughs at Co and Ni (Table 4, Fig. 6a).

Amphibole

Though not as abundant as pyroxene, amphibole macrocrysts are nonetheless widespread with a similar size distribution and strong pleochroism, from the reddish brown to yellow brown colour. Most amphibole macrocrysts exhibit subrounded shapes and embayment features, and commonly are partially or completely surrounded by reaction coronas of variable thickness (200-700 µm thick), which may be wrapped in some places by the groundmass foliation defined by plagioclase microlites. The coronas consist of an assemblage of fine-grained minerals including ilmenite + plagioclase ± clinopyroxene ± rhönite (Fig. 7a, b). The grain size of these coronas increases with the width of the corona. The reaction coronas may appear as a worm-like symplectite or as a boxy-like intergrowth where pyroxene crystals show the same optical orientation and are elongated parallel to the kaersutite c-axis. Amphiboles with thin opaque-rich coronas (< 50 µm) along the contact with the groundmass can be also observed. The reaction coronas do not develop where amphibole is in contact with another mineral phase. Unlike clinopyroxenes, the individual macrocrysts of kaersutite are compositionally relatively homogeneous with narrow ranges in MgO (11.77-12.45 wt%; 12.43 ± 0.47 wt%), Al_2O_3 (14.10-15.30 wt%; avg. 14.67 ± 0.27 wt%), TiO_2

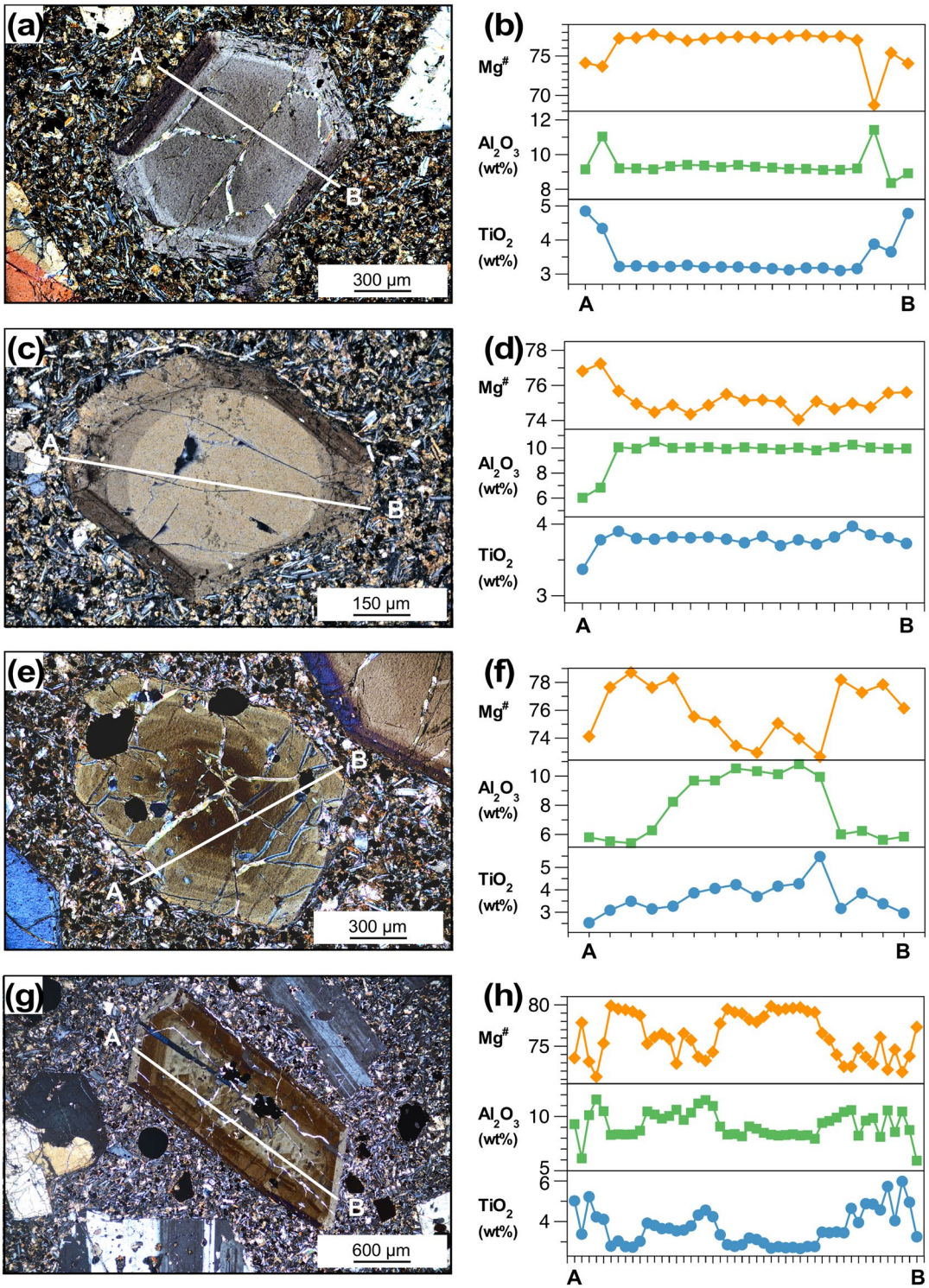

Fig. 4 **a** Light brown euhedral clinopyroxene macrocryst that is encapsulated by a pinkish-brown rim displaying sector zoning and numerous minute inclusions of the groundmass. **b** Compositional profile corresponding to the pyroxene of **a**. **c** Euhedral pyroxene macrocryst including a rounded core and a mantle truncated by a rim displaying sector zoning. **d** Compositional profile corresponding to the pyroxene of **c**. **e** Euhedral clinopyroxene macrocryst with concentric, oscillatory zoning towards the rim. **f** Compositional profile corresponding to the pyroxene of **e**. **g** Euhedral macrocryst that includes a core with intricacy zoning, mantled by a zone showing low frequency oscillations and a rim with sector zoning. **h** Compositional profile corresponding to the pyroxene of **g**. **i** Resorbed clinopyroxene macrocryst with a relatively homogeneous core and a thin Mg-rich rim displaying a ragged fibrous contact with the groundmass. **j** Compositional profile corresponding to the pyroxene of **i**. **k** Clinopyroxene macrocryst with strong external and internal resorption. **l** Pyroxene macrocryst consisting of a core pseudomorphed by a brown crystal patchwork and a euhedral overgrowth

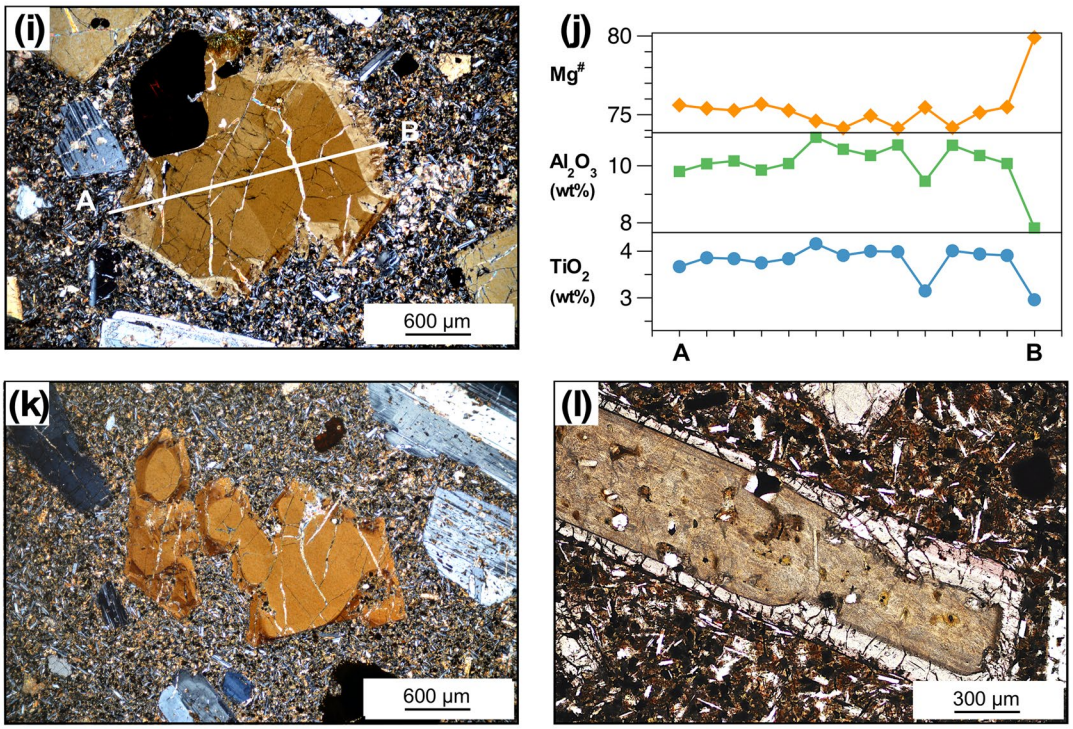

Fig. 4 (continued)

(6.65-7.04 wt%; avg. 6.78 ± 0.11 wt%) and FeOtot (8.50-11.68; avg. 9.72 ± 0.55 wt%) (Table 5). Mössbauer spectroscopy of three amphibole samples reveal a Fe^{3+}/Fetot ratio of 0.35-0.37. Based on the nomenclature of Hawthorne et al. (2012) amphiboles can be described as kaersutite with Ti > 0.5 apfu, and it should be considered as an oxo-amphibole with dominant O^{2-} in the W-site, not as a ^{W}(OH, F, Cl)-dominant calcium-bearing amphibole. Accordingly, if Ti = 1.17 - 0.52(OH+F) (Hawthorne et al. 1998), the amount of $^{W}O^{2-}$ in the studied amphibole macrocrysts is in the range of 1.20 to 1.27 (Table 5). Overall, the contents of Fe^{3+} inferred from (OH+F) values (Popp et al. 2006) are reasonably in agreement with the Mössbauer data. Mg# values vary in the range of 0.68-0.72 (avg. 0.70 ± 0.02), which are similar to other occurrences of kaersutite macrocrysts in basalts of the Basque-Cantabrian Basin (≤ 0.70, Azambre et al. 1992).

Some macrocrysts reveal significant small compositional variations in Mg# (up to 3.5) with a general increase toward the rims. Other elements such as Al_2O_3 show minor to trifling variations. Al_2O_3/TiO_2 and Na_2O/K_2O ratios as well as Mg# values, around 2.15, 0.78 and 70 respectively, are consistent with the composition of amphiboles from intraplate basalts and OIB (Fig. 2b, c,). However, amphiboles of this study have higher TiO_2 contents (around 6.80 wt%) than those from lithospheric veins, metasomatised peridotites and continental basanites (Fig. 7c) (< 6.0 wt% TiO_2, Pilet et al. 2008). Trace-elements and REE concentrations determined by LA-ICP-MS are homogeneous with no significant variations between different samples and macrocrysts (Table 4). In relation to the primitive mantle, amphiboles from this study are enriched in Rb, Ba, Sr, REE+Y and HFSE's except TE's, with a concave downward REE pattern, positive (Ti, Nb, Ta) and negative (Th, U, Pb) anomalies (Fig. 6b). The Nb/Th and Lu/Hf ratios are in the ranges of 250-475 and 0.04-0.07 (Fig. 6c), respectively, which are akin to compositions given for amphiboles from metasomatic veins within the lithosphere (Ionov and Hoffmann 1995; Witt-Eickschen et al. 2003; Powell et al. 2004). Trace-element abundances between coexisting amphibole and clinopyroxene (Fig. 6d) are like those reported in previous studies (Ionov and Hoffmann 1995; Powell et al. 2004), with an enrichment of Rb, Ba, Pb, Sr, Ti, Nb and Ta in amphibole over clinopyroxene.

Other minerals

Rhönite typically occurs around resorbed kaersutite macrocrysts, commonly forming part of coronas with plagioclase + clinopyroxene + ilmenite (Fig. 7a, b). It is very fine-to fine-grained (< 400 µm), with a subhedral to skeletal habit and a dark-reddish brown to black coloured. Microprobe analysis reflects a narrow compositional range: 22.90-24.10 wt% SiO_2, 11.56-12.94 wt% TiO_2, 15.84-17.01 wt% Al_2O_3, 19.49-21.78 wt% FeOtot, 12.68-14.09 wt% MgO, 11.13-12.28 wt% CaO, 0.73-0.89 wt% Na_2O (Table 6). Rhönite of this study deviates significantly of the ideal rhönite composition (Bonaccorsi et al.1990, Kunzmann 1999) (see Fig. S2 in electronic supplementary material), and strong correlations

Table 3 Selected chemical compositions, calculated mineral formulae and calculated end-member fractions for clinopyroxene

Sample nº	1	2	3	4	5	6	7	8	9	10	11	12
Zone	Cores						Rims					
Major oxides (wt%)												
SiO_2	45.77	46.47	44.35	43.38	46.56	44.78	42.55	42.17	41.85	46.10	46.97	42.93
TiO_2	2.79	2.53	3.55	3.91	2.42	3.18	5.02	4.86	5.48	2.96	3.07	4.78
Al_2O_3	8.30	8.05	9.19	10.08	7.92	9.18	9.29	9.85	10.18	7.82	5.87	8.92
Cr_2O_3	0.10	0.27	0.09	0.02	0.41	0.06	0.03	0.03	0.03	0.13	0.02	0.02
FeO*	3.16	3.41	4.35	4.08	3.40	3.79	4.49	4.46	4.51	3.82	4.92	4.23
Fe_2O_3*	3.12	2.83	2.61	3.16	2.85	3.03	3.16	3.43	3.06	2.51	2.33	3.47
MnO	0.13	0.11	0.10	0.11	0.11	0.09	0.12	0.11	0.13	0.09	0.15	0.09
MgO	13.28	13.50	12.38	11.97	13.55	12.69	11.45	11.37	11.32	13.56	13.32	11.77
CaO	22.52	22.41	22.19	22.17	22.36	22.23	22.71	22.63	22.62	22.27	22.51	22.94
Na_2O	0.52	0.52	0.45	0.55	0.52	0.52	0.49	0.44	0.45	0.41	0.41	0.47
K_2O	0.02	0.02	0.03	0.02	0.02	0.01	0.01	0.02	0.03	0.03	0.01	0.02
F	0.16	0.16	0.13	0.13	0.16	0.16	0.18	0.19	0.16	0.15	0.21	0.12
Cl	0.01	bdl	0.01	0.01	bdl	0.01	0.01	bdl	bdl	bdl	bdl	bdl
O=F+Cl	0.07	0.07	0.06	0.06	0.07	0.07	0.08	0.08	0.07	0.06	0.09	0.05
Total	99.80	100.21	99.37	99.54	100.20	99.66	99.43	99.48	99.76	99.79	99.68	99.71
Calculated mineral formulae (apfu)*												
Si	1.703	1.720	1.666	1.630	1.723	1.673	1.612	1.597	1.580	1.716	1.759	1.620
$Al^{(IV)}$	0.297	0.280	0.334	0.370	0.277	0.327	0.388	0.403	0.420	0.284	0.241	0.380
$Al^{(VI)}$	0.067	0.071	0.073	0.076	0.069	0.077	0.026	0.037	0.034	0.059	0.019	0.017
Ti	0.078	0.070	0.100	0.110	0.067	0.089	0.143	0.138	0.156	0.083	0.086	0.136
Cr	0.003	0.008	0.003	0.001	0.012	0.002	0.001	0.001	0.001	0.004	0.001	0.001
Fe^{3+}	0.087	0.079	0.074	0.089	0.079	0.085	0.090	0.098	0.087	0.070	0.066	0.099
Fe^{2+}	0.098	0.106	0.137	0.128	0.105	0.118	0.142	0.141	0.143	0.119	0.154	0.133
Mg	0.736	0.745	0.693	0.670	0.747	0.707	0.646	0.642	0.637	0.752	0.743	0.662
Mn	0.004	0.003	0.003	0.004	0.003	0.003	0.004	0.004	0.004	0.003	0.005	0.003
Ca	0.898	0.889	0.893	0.892	0.887	0.890	0.922	0.918	0.915	0.888	0.904	0.928
Na	0.038	0.037	0.033	0.040	0.037	0.038	0.036	0.032	0.033	0.030	0.030	0.034
K	0.001	0.001	0.001	0.001	0.001	0.000	0.000	0.001	0.001	0.001	0.001	0.001
F	0.019	0.019	0.016	0.016	0.019	0.019	0.022	0.023	0.019	0.018	0.025	0.014
Cl	0.001	0.000	0.001	0.001	0.000	0.001	0.001	0.000	0.000	0.000	0.000	0.000
Calculated end-member fractions (mol%)												
Wo	49.23	48.80	49.62	50.03	48.67	49.36	51.09	50.94	51.24	48.47	48.28	50.84
En	40.38	40.89	38.51	37.57	41.02	39.19	35.83	35.60	35.67	41.05	39.72	36.28
Fs	10.39	10.32	11.87	12.40	10.31	11.46	13.08	13.46	13.09	10.48	12.00	12.87

* Calculated based on 6 O atoms per formula unit, FeO*and Fe_2O_3* calculated for electroneutrality

bdl below detection limit

of (Ca+Na) vs. (Si+Na) and (Ti+R^{2+}) vs. Fe^{3+} indicate that exchange vectors $(AlCa)(SiNa)_{-1}$ and $(Fe^{3+})_2(Ti+R^{2+})_{-1}$ are the main causes of the compositional deviation. High (Na + ^{IV}Si) and low (Ca + ^{IV}Al) is characteristic of rhönite formed as a breakdown product of kaersutite (Grapes et al. 2003). By comparison, the rhönite composition of Armintza is similar to that of rhönites from alkali basalts (e.g., Kong et al. 2020), but has higher (Ca + ^{IV}Al) and lower (Na + ^{IV}Si) than rhönites from pyroxenite xenoliths (Grapes et al. 2003). However, there is significant compositional overlap and there does not appear to be a clear relationship between composition and mode of occurrence.

Ilmenite is the only oxide component observed in the basaltic lava flow. It is relatively abundant and may present as: (1) subhedral to rounded crystals (mostly < 3 mm) associated to ferromagnesian minerals; (2) acicular (< 30 μm) crystals included within amphibole; or (3) small subrounded grains (< 40 μm) forming part of the groundmass. Ilmenite has a significant MgO content (1.07 to 7.70 wt%) and contains minor amounts of MnO (0.38 to 0.76 wt%) (Table 6) Some ilmenite crystals display a lamellar microstructure where Mg-poor lamellae (≈ 0.20-1.0 wt%) alternate with Mg-rich lamellae (4.80-7.70 wt%).

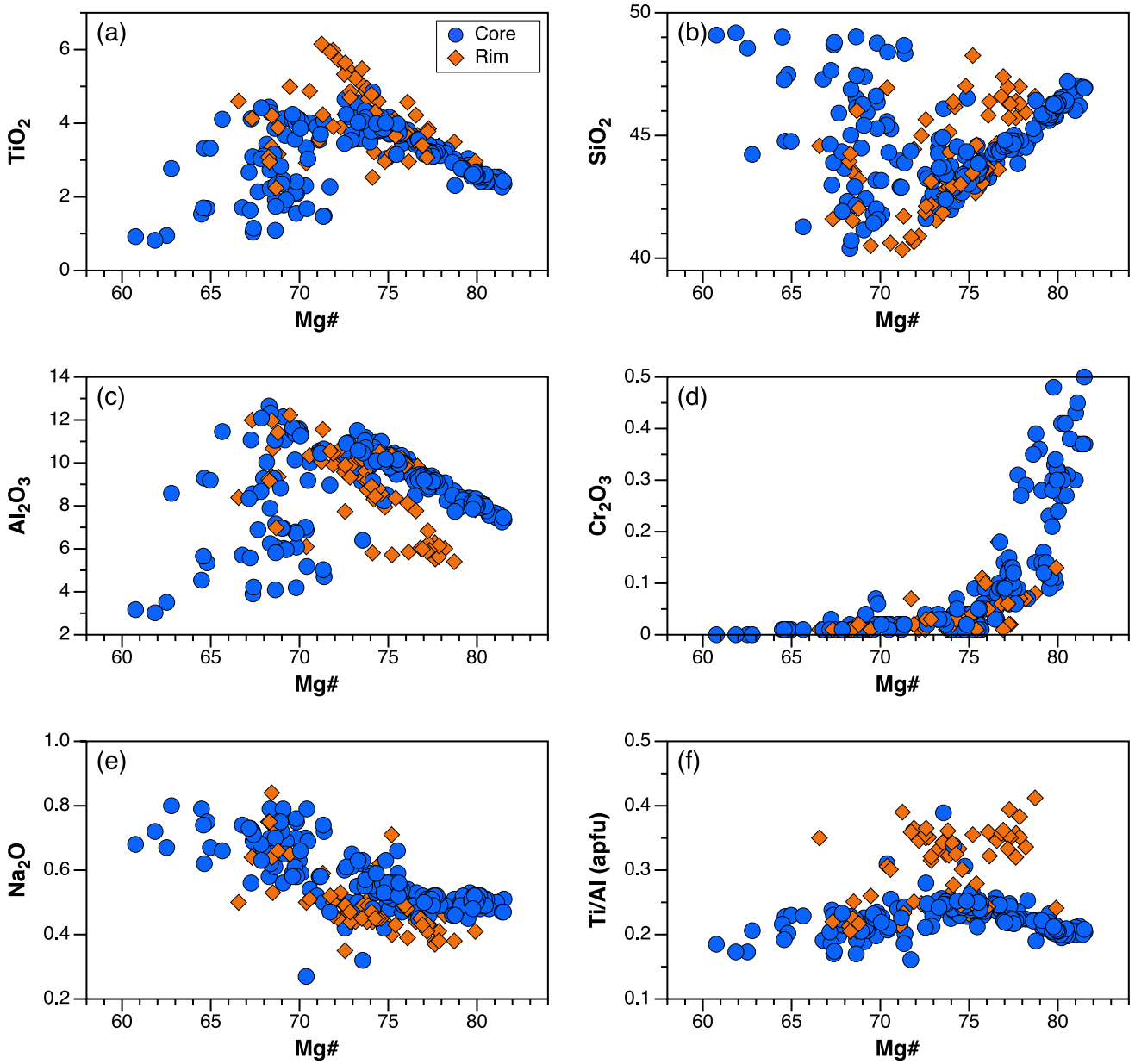

Fig. 5 Compositional variations of clinopyroxene macrocrysts from the Armintza pillow-lava in terms of Mg# vs. major elements (**a**, **b**, **c**, **d**, **e**) and Ti/Al ratios (**f**)

Apatite is a relatively common accessory phase that occurs in the groundmass and as inclusions in clinopyroxene and amphibole, showing a prismatic-columnar habit and variable grain size (up to 1 mm, but mostly < 660 µm parallel to the c-axis). It is fluorapatite with F (2.08-2.78 wt%), Cl (0.38-0.45 wt%), FeO (0.25-0.34 wt%), MgO (0.20-0.40 wt%) and MnO (0.04-0.09 w.t%). Pyrrhotite ($Fe_{1-x}S$) with x = 0.89 to 0.99 occurs in some samples.

Discussion

Inferences from the mineral textures and composition

Plagioclase

Complex zoning patterns and the variety of crystal morphologies in plagioclase macrocrysts, with internal and external

Table 4 Trace element concentrations (ppm) of clinopyroxene and amphibole

Sample nº	1	2	3	4	5	6	7	8	9	10	11	12	13	14	15
	Px						Amp								
Li	0.6	0.6	0.7	0.6	0.6	0.6	1.9	0.8	1.5	0.6	5.8	1.5	5.1	1.9	0.9
Be	0.6	0.3	0.4	0.6	0.3	0.4	0.5	0.6	0.5	0.4	0.3	0.3	0.2	0.4	0.3
P	14.8	27.9	19.9	20.7	36.4	29.8	40.4	50.2	53.6	52.7	62.4	149.4	99.4	60.0	151.5
Sc	59.7	82.8	52.9	83.9	64.3	76.4	52.0	46.6	53.7	41.6	41.3	31.7	45.6	52.7	20.8
V	400.8	393.3	405.0	429.6	505.4	403.7	549.8	557.9	569.9	560.3	673.3	620.6	583.5	602.2	591.3
Cr	34.8	233.1	7.3	421.0	102.3	1160.7	31.6	17.0	61.4	9.7	32.9	153.6	15.3	14.4	1.9
Co	19.4	25.1	17.3	32.4	19.8	31.0	47.6	43.6	49.8	40.3	23.3	32.7	31.6	41.1	24.6
Ni	6.0	23.9	4.1	69.3	24.9	85.1	35.3	18.6	46.4	12.3	18.3	15.9	7.9	14.0	3.4
Cu	1.2	1.1	1.3	1.4	1.8	52.5	2.2	2.2	2.1	2.0	3.5	2.2	5.3	2.5	2.5
Zn	22.2	20.8	20.9	20.9	25.3	21.6	33.2	35.8	35.3	36.0	24.3	40.0	43.2	36.0	55.2
Ga	15.9	15.7	16.4	16.6	17.4	13.4	14.1	15.3	14.8	15.2	18.1	14.8	15.4	15.0	15.6
Rb	bdl	0.1	0.1	bdl	0.01	bdl	15.6	16.1	15.6	15.8	16.3	13.8	16.9	16.5	13.3
Sr	117.4	114.3	124.3	108.1	142.8	114.6	772.0	831.9	775.8	848.4	923.6	1551.6	862.2	847.7	1459.9
Y	11.3	11.7	12.2	9.9	11.9	9.6	8.9	10.4	9.2	10.8	9.3	12.9	10.1	10.1	14.5
Zr	72.3	72.3	77.6	61.4	69.4	54.8	35.8	41.1	35.3	42.0	37.2	43.2	39.6	38.7	54.7
Nb	1.1	1.1	1.2	0.9	1.3	0.8	21.0	22.8	21.6	23.7	24.3	29.9	22.6	22.5	35.6
Ba	0.4	0.8	1.7	0.2	0.4	0.1	755.9	803.3	767.1	779.7	789.4	956.7	792.5	804.5	1030.2
La	5.96	6.12	6.28	5.61	6.58	4.87	6.62	8.10	7.21	7.58	8.15	8.25	7.59	7.22	10.13
Ce	20.97	21.30	21.23	20.98	24.05	17.69	22.55	25.41	23.55	24.42	26.81	28.72	23.48	23.72	34.66
Pr	3.67	3.58	3.78	3.57	4.00	2.87	3.66	4.04	3.66	4.06	4.01	4.61	3.65	3.45	5.51
Nd	18.74	20.24	22.28	19.48	20.92	16.69	17.39	21.52	19.55	20.99	20.03	24.29	19.42	18.79	30.66
Sm	5.15	4.70	4.88	4.71	5.51	4.25	4.32	5.06	4.52	4.64	4.62	5.77	4.71	4.76	6.97
Eu	1.85	1.88	1.98	1.74	1.98	1.43	1.31	1.57	1.49	1.60	1.46	2.07	1.55	1.42	2.32
Gd	3.98	4.32	3.94	3.58	4.17	3.32	3.42	3.99	3.25	3.79	3.72	4.61	3.31	3.25	5.33
Tb	0.61	0.60	0.59	0.51	0.66	0.50	0.46	0.56	0.41	0.50	0.52	0.65	0.52	0.43	0.78
Dy	2.95	3.05	3.34	2.60	2.93	2.60	2.27	3.05	2.54	2.46	2.43	3.35	2.60	2.48	3.50
Ho	0.48	0.51	0.62	0.46	0.52	0.44	0.38	0.49	0.40	0.49	0.37	0.59	0.43	0.39	0.58
Er	1.18	1.37	1.15	1.12	1.17	0.93	0.99	1.12	0.88	1.06	1.01	1.15	0.85	0.82	1.45
Tm	0.17	0.13	0.16	0.12	0.13	0.11	0.13	0.11	0.11	0.11	0.10	0.15	0.13	0.10	0.20
Yb	0.84	0.88	0.93	0.93	0.92	0.97	0.76	0.83	0.65	0.70	0.76	0.85	0.66	0.84	0.88
Lu	0.12	0.11	0.09	0.08	0.12	0.07	0.09	0.10	0.10	0.10	0.10	0.10	0.09	0.08	0.09
Hf	3.58	3.86	3.71	3.19	3.08	2.61	1.41	2.34	1.49	2.00	1.53	1.65	1.72	1.61	2.08
Ta	0.21	0.22	0.28	0.21	0.27	0.13	1.28	1.36	1.16	1.30	1.24	1.31	1.22	1.15	1.54
Pb	0.10	0.08	0.13	0.03	0.04	0.06	0.31	0.19	0.37	0.36	0.34	0.29	0.69	0.22	0.31
Th	0.09	0.1	0.12	0.08	0.09	0.03	0.08	0.07	0.07	0.05	0.07	0.07	0.05	0.07	0.07
U	0.01	0.02	0.01	0.02	0.02	0.01	0.03	0.01	0.08	0.01	0.01	0.01	0.01	0.01	0.01

bdl below detection limit

resorption events, are interpreted to result from changes in physical and chemical conditions of the magma. Convolute and oscillatory zoning in plagioclase characterised by oscillations of variable frequency and amplitude in An content, together with minor and major resorption surfaces, may be indicative of feedback processes involving grain nucleation, growth, replacement and dissolution (Pearce and Kolisnik 1990). Resorption events that involve only changes in An-content might be attributed to closed-system processes, such as: (i) convective self-mixing within a system with temperature and H_2O gradients (Couch et al. 2001); (ii) temperature increase of ascending magma provoked by the release of

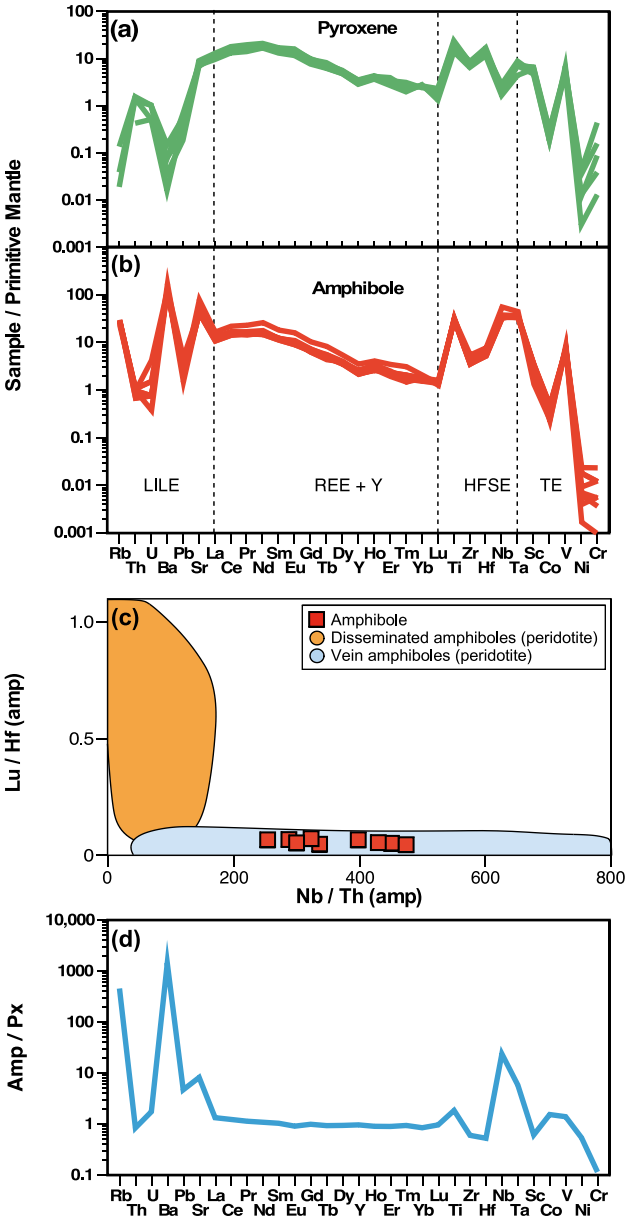

Fig. 6 **a** Trace-element concentrations for pyroxenes (normalised to primitive mantle, McDonough and Sun 1995). **b** Trace-element concentrations of amphiboles (normalised to primitive mantle, McDonough and Sun 1995). **c** Nb/Th vs. Lu/Hf for studied amphiboles in relation with disseminated and vein amphiboles from mantle xenoliths and magmatic pyroxenite veins (Ionov and Hoffmann 1995; Witt-Eickschen et al. 2003). **d** Trace element partitioning between amphibole and clinopyroxene from the basaltic pillow lava of Armintza

latent heat, resulting in the increase of the An content during plagioclase crystallization (Blundy et al. 2006); or (iii) decompression of a H_2O-undersaturated magma shifting the composition of plagioclase towards the calcic end, which can lead to resorption and sieve textures in plagioclase (Nelson and Montana 1992). However, if decompression was the main cause of resorption textures the entire volume of the magma would be affected, and hence all macrocrysts would have undergone similar degrees of dissolution. In addition, the juxtaposition of texturally and compositionally distinct plagioclase populations within single samples would be difficult to explain by decompression, or by the release of latent heat of crystallization.

Complex zoning patterns and resorption features in plagioclase might be due to open-system processes such as magma recharge and mixing. Sieve textures in plagioclase have been experimentally reproduced and may be indicative of dissolution driven by injection of hotter Ca-rich melt (Tsuchiyama 1985; Nakamura and Shimakita 1998). Experimental works of Tsuchiyama (1985) show that incorporation of plagioclase into a melt with which it is not in equilibrium can give rise to: (1) mantled crystals if plagioclase is less anorthitic than the plagioclase which is in equilibrium with the melt; or (2) partial melting if the temperature of melt is greater than the solidus temperature of the introduced plagioclase. The injection of a hotter magma, e.g. during more mafic magma recharge, would drive melting or dissolution of plagioclases that are no longer in equilibrium with the host melt. Equilibrium plagioclase compositions have been calculated using the model of Takagi et al. (2005) for a range of pressures, temperatures and water contents. Accordingly, expressing the degree of disequilibrium as ΔAn (measured An - calculated An), ΔAn values of -15.2 to 3.25 and -29.0 to 4.5 are obtained for rims and cores, respectively, which indicates a significant disequilibrium between plagioclase and melt (see Fig. S3 in electronic supplementary material).

Ruprecht and Wörner (2007) postulated that while variations in An alone are not indicative of closed- or open-system processes, compositional variations in Fe, Mg and Ti across major resorption interfaces can be used to distinguish both processes. The concentration of these elements in plagioclase mainly depends on bulk composition (Ginibre et al. 2002), and their partition coefficients are a function of the An content, temperature, oxygen fugacity, H_2O content and, to a lesser extent, pressure (Bindeman and Davis 2000; Tepley et al. 2010; Dohmen and Blundy 2014; Sun et al. 2017). Fe partitioning strongly depends on fO_2 (Wilke and Behrens 1999; Sugawara 2000, 2001), so that Fe is mainly incorporated into plagioclase as Fe^{3+} at high fO_2, replacing Al^{3+}, and increases with the An content. Fe and Ti in plagioclase mostly show positive to flat or weakly negative trends with the An content (Fig. 8a). The positively correlated trend for An and Fe is difficult to explain only by changes in fO_2 or fH_2O, suggesting the involvement of other processes. According to Ruprecht and Wörner (2007), the positive An-Fe trend would reflect the effects of open-system evolution with recharge and compositional mixing, while the subhorizontal trend of Fe and decreasing Mg with increasing An would be consistent with closed-system

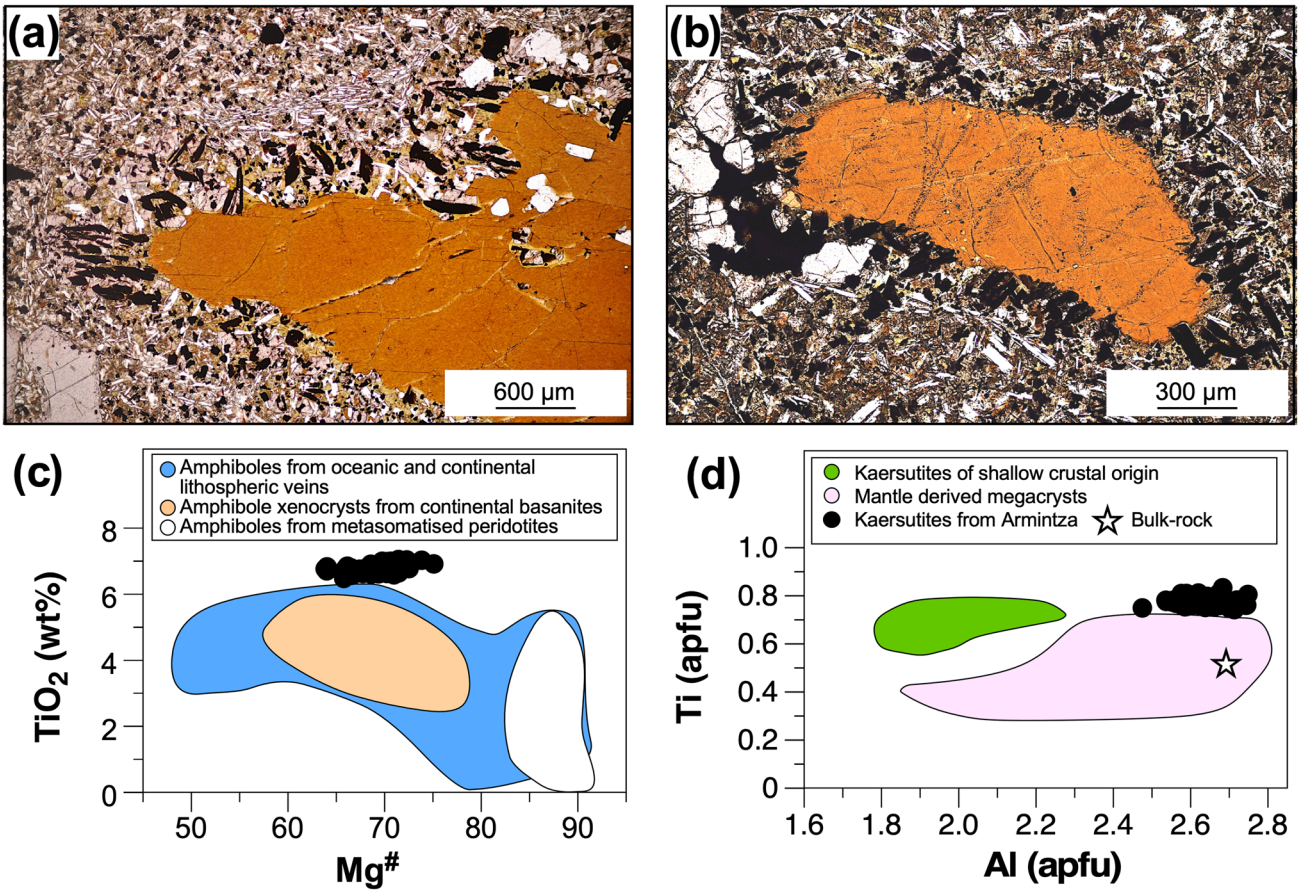

Fig. 7 **a** Corona of rhönite + clinopyroxene + plagioclase microlites and ilmenite on kaersutite. **b** Subrounded kaersutite with a corona of rhönite + plagioclase **c** Mg# versus TiO_2 contents for amphiboles of this study relative to amphiboles from lithospheric veins, basanites and metasomatised peridotites. **d** Ti (apfu) versus Al (apfu) for amphiboles of this study (black circles) relative to crustal kaersutites (green) and mantle-derived kaersutites (pink) recorded by Best (1974)

evolution involving only thermal effects and decompression. Unlike Fe and Ti, K_DMg in plagioclase weakly correlates with An content (Bindeman et al. 1998), but An-Mg data show a trend similar to An-Fe (Fig. 8a), which suggests a little influence of fO_2 on variations of Fe in plagioclase. Since the TiO_2 content is relatively insensitive to pressure changes ((0.01/GPa, Bedard 2006), the ΔTiO_2 values across the resorption surfaces would remain constant during decompression. Instead, magma recharge and mixing would be characterised by negative values for both ΔAn and ΔTiO_2, as well as for ΔFeO and ΔMgO (Fig. 8b).

Plagioclase glomerocrysts are interpreted as disaggregated fragments of a crystal-rich layer (mushy layer) entrained by the ascending melt. Some of them are encompassed by thin rims (< 50 μm) relatively rich in Fe-Mg-Ti, suggesting that they formed after the disturbance and breakage of the crystal-rich layer due to magma recharge. Regarding the microlites, these were likely formed by decompression and degassing during ascent of the magma to the surface, and their narrow range in size suggests a rapid cooling (Mangler et al. 2022).

Clinopyroxene

Resorption, zoning patterns and compositional variation in clinopyroxenes could be attribute to three main processes. (1) Decompression that may account for the occurrence of resorbed cores mantled by overgrowths with higher Mg# contents. Phase-equilibrium experiments at constant temperature and water content (although for different compositions) suggest that decreasing pressure in a water-undersaturated melt results in an increase of the Mg content of pyroxenes (Solaro et al. 2019). The onset of crystallization of amphibole coupled with decompression can also give rise to reverse zoning in pyroxenes (e.g. Pe-Piper 1984). However, as in the case of plagioclase, if decompression was the triggering factor of Mg enrichment, all neighbouring pyroxene macrocrysts would be expected to have reverse zonation. On

Table 5 Selected chemical compositions and calculated mineral formulae for amphibole

Sample nº	1	2	3	4	5	6	7	8	9	10	11	12
Major oxides (wt%)												
SiO_2	38.06	38.60	37.80	37.18	38.05	38.76	37.40	38.47	37.62	37.59	37.77	37.85
TiO_2	6.93	6.98	6.79	6.75	6.77	6.80	6.79	6.77	6.80	6.90	6.77	6.76
Al_2O_3	14.89	14.79	14.47	15.31	14.93	14.71	14.99	14.40	14.85	14.86	14.87	14.59
FeO*	5.40	6.14	6.02	7.30	6.59	7.86	6.51	8.08	6.75	6.64	6.50	6.55
Fe_2O_3*	3.74	3.72	3.52	3.46	3.38	3.48	3.52	3.47	3.52	3.74	3.47	3.47
MnO	0.04	0.10	0.09	0.07	0.09	0.19	0.08	0.19	0.07	0.04	0.10	0.11
MgO	12.60	12.92	13.01	12.08	12.99	11.00	12.64	11.24	12.39	12.25	12.54	12.67
CaO	12.46	12.51	12.35	12.32	12.34	12.13	12.35	11.94	12.47	12.37	12.12	12.37
Na_2O	1.74	1.64	1.63	1.74	1.73	2.14	1.71	2.34	1.86	1.66	1.78	1.53
K_2O	2.30	2.30	2.26	2.07	2.23	1.72	2.15	1.75	2.17	2.19	2.15	2.14
F	0.14	0.14	0.34	0.36	0.33	0.08	0.27	0.17	0.28	0.08	0.11	0.26
Cl	0.01	0.03	0.02	0.03	0.04	0.03	0.05	0.02	0.01	0.01	0.03	0.02
H_2O*	0.66	0.68	0.59	0.59	0.62	0.72	0.62	0.68	0.62	0.69	0.70	0.64
O=F+Cl	0.06	0.07	0.15	0.16	0.15	0.04	0.12	0.07	0.12	0.04	0.05	0.11
Total*	98.91	100.50	98.74	99.09	99.94	99.58	98.96	99.44	99.30	98.98	98.87	98.82
Calculated mineral formulae (apfu)*												
Si	5.729	5.735	5.719	5.633	5.694	5.831	5.660	5.812	5.679	5.689	5.707	5.726
$Al^{(IV)}$	2.271	2.265	2.281	2.367	2.306	2.169	2.340	2.188	2.321	2.311	2.293	2.274
$Al^{(VI)}$	0.371	0.325	0.300	0.367	0.327	0.439	0.333	0.375	0.321	0.340	0.355	0.328
Ti	0.785	0.781	0.773	0.769	0.762	0.769	0.773	0.769	0.772	0.786	0.770	0.769
Fe^{3+}	0.424	0.416	0.401	0.394	0.380	0.394	0.401	0.394	0.400	0.426	0.395	0.395
Fe^{2+}	0.680	0.763	0.762	0.925	0.825	0.989	0.824	1.021	0.853	0.841	0.821	0.828
Mg	2.827	2.863	2.935	2.729	2.898	2.467	2.852	2.532	2.789	2.764	2.825	2.858
Mn	0.006	0.012	0.012	0.009	0.011	0.025	0.010	0.025	0.010	0.006	0.013	0.014
Ca	2.009	1.992	2.002	2.000	1.979	1.956	2.002	1.933	2.017	2.007	1.963	2.004
Na	0.507	0.473	0.478	0.511	0.502	0.625	0.502	0.041	0.544	0.487	0.521	0.448
K	0.441	0.437	0.436	0.400	0.426	0.331	0.415	0.337	0.417	0.422	0.414	0.414
F	0.068	0.067	0.164	0.174	0.157	0.040	0.130	0.080	0.136	0.041	0.055	0.124
Cl	0.004	0.007	0.005	0.008	0.010	0.007	0.013	0.006	0.003	0.004	0.008	0.004
OH	0.673	0.682	0.600	0.597	0.627	0.731	0.633	0.691	0.629	0.698	0.715	0.646
O	1.255	1.244	1.231	1.222	1.205	1.223	1.223	1.224	1.232	1.257	1.222	1.226

* Calculated based on 24 (O, OH,F, Cl) atoms per formula unit, FeO*and Fe_2O_3* calculated (Popp et al. 2006)

the contrary, a diversity of textures and compositional trends are found at thin-section scale. (2) Convective self-mixing in a magma body of single composition heated from below can bring about crystal circulation driven by compositional and thermal gradients in magma reservoir, and thus explain the disequilibrium features in pyroxenes and mixing of crystals with different thermal histories (Couch et al. 2001; Ginibre et al. 2002). Assuming that bulk rock composition represents the melt composition, we have explored for equilibrium using the model of Mollo et al. (2013) based on the difference between diopside + hedenbergite (ΔDi+Hd) components predicted for clinopyroxene and those observed in analysed crystals, showing a significant disequilibrium in general (see Fig. S4a in electronic supplementary material). This could be due in part to the fact that the samples analysed have relatively high Mg# values as a consequence of a significant content of antecrysts in the rock, as suggested by Ubide et al. (2014b) (3) Magma recharge and mixing, even with the incorporation of crystals from new batches of hotter magma into the system, can give rise to breakage, resorption and crystal dissolution leading to complex crystal fabrics and zoning in pyroxenes. Evidence for magma recharge and mixing is supported by the occurrence of overgrowths or mantles with higher Mg contents, oscillatory zoning in macrocrysts with low amplitude oscillations, resorption surfaces and saw-tooth zones (e.g. Streck 2008; Coote and Shane 2018). There are crystals, however, with a Mg drop in the outermost parts of the rims that may be indicative of some fractionation after the magma recharge. Although patchy zoning may be produced by intra-crystal

Table 6 Selected chemical compositions and calculated mineral formulae for rhönite and ilmenite

Sample nº	1	2	3	4	5	6	7	8	9	10	11	12
	Rhönite						Ilmenite					
Major oxides (wt%)												
SiO_2	23.61	23.35	23.26	23.40	22.69	23.41	0.02	0.01	0.02	0.03	0.02	0.22
TiO_2	11.68	11.82	12.51	11.70	12.57	11.56	48.28	45.77	47.84	50.80	50.19	49.75
Al_2O_3	16.22	16.37	16.60	16.80	16.26	16.27	1.10	0.85	1.08	0.48	0.23	0.50
Cr_2O_3	na	na	na	na	na	na	0.03	0.04	bdl	bdl	0.01	0.04
Fe_2O_3*	8.38	9.30	7.39	8.97	9.15	9.33	14.59	17.56	14.25	6.42	6.33	6.28
FeO*	13.54	12.59	14.51	12.70	12.94	13.03	29.37	29.40	29.84	36.72	40.27	41.12
MnO	0.19	0.24	0.13	0.21	0.17	0.17	0.38	0.40	0.43	0.39	0.29	0.25
MgO	13.16	13.52	12.65	13.13	13.13	13.24	7.70	6.41	7.13	4.79	2.54	2.07
CaO	11.90	12.11	12.01	12.28	12.23	12.04	0.04	0.04	0.05	0.06	0.07	0.05
Na_2O	0.82	0.83	0.83	0.90	0.84	0.82	bdl	bdl	bdl	bdl	bdl	bdl
K_2O	0.05	0.01	0.10	0.01	0.01	0.02	bdl	bdl	bdl	bdl	bdl	bdl
Total	99.55	100.13	99.99	100.11	100.00	99.69	101.51	100.48	100.65	99.68	99.94	100.28
Calculated mineral formulae (apfu)*												
Si	6.398	6.286	6.291	6.296	6.140	6.328	0.001	0.001	0.001	0.001	0.001	0.005
$Al^{(IV)}$	5.182	5.195	5.295	5.329	5.185	5.185						
$Al^{(VI)}$							0.032	0.025	0.032	0.014	0.007	0.015
Cr							0.001	0.001	bdl	bdl	0.000	0.001
Ti	2.380	2.393	2.544	2.368	2.558	2.350	0.893	0.874	0.895	0.952	0.956	0.945
Fe^{3+}	1.709	1.883	1.505	1.817	1.864	1.897	0.258	0.318	0.255	0.118	0.118	0.117
Fe^{2+}	3.068	2.833	3.282	2.859	2.929	2.944	0.578	0.591	0.594	0.750	0.836	0.852
Mg	5.315	5.424	5.101	5.266	5.295	5.333	0.282	0.243	0.264	0.178	0.096	0.078
Mn	0.044	0.055	0.030	0.049	0.040	0.039	0.008	0.009	0.009	0.008	0.006	0.005
Ca	3.455	3.493	3.481	3.542	3.544	3.487	0.001	0.001	0.001	0.001	0.002	0.003
Na	0.431	0.433	0.436	0.472	0.443	0.430	-	-	-	-	-	-
K	0.017	0.003	0.035	0.002	0.002	0.007	-	-	-	-	-	-

*Calculated based on assuming 28 cations and 40 O atoms in rhönite and 3 O atoms per formula unit in ilmenite, FeO*and Fe_2O_3* calculated for electroneutrality

bdl below detection limit, *na* not analysed

diffusional processes over time (Tomiya and Takahashi 2005), or also by melt-reequilibrium processes of originally unzoned crystals which are in disequilibrium with the host magma (Streck 2008), in light of textural overlap and compositional variation we interpret patchy zoning as a result of disequilibrium induced by open system processes.

Amphibole

The lack of a clear zonation with indistinct zoning patterns in amphibole contrasts with the textures and compositional variation of plagioclase and clinopyroxene. However, like clinopyroxenes, amphibole compositions mostly fall below the range in which mineral and melt compositions are in equilibrium (see Fig. S4b in electronic supplementary material), based on the $Kd^{amph\text{-}melt}_{Fe\text{-}Mg} = 0.38 \pm 0.05$ (LaTourrettte et al. 1995). Many kaersutite macrocrysts show rounding, strong embayment and breakdown features that commonly manifest into the formation of coronas or rims of variable thickness produced by amphibole-melt reaction. There are two possible explanations for these features. (1) Decompression-induced breakdown reactions, particularly for the thin opaque-rich rims, during magma ascent from the storage zone at depth (Rutherford and Hill 1993; Rutherford and Devine 2003), where rim width would depend on time, degree of disequilibrium in P and T, and decompression rate. In this context, the occurrence of partially rimmed amphiboles could represent fragments that disaggregated during upflow of magma. (2) Magmatic recharge giving rise magma heating and high temperature amphibole destabilization. This would be consistent with the occurrence of strongly resorbed amphiboles showing width reaction coronas and the juxtaposition within a single sample of fresh unrimmed and rimmed amphiboles. In contrast to reaction rims produced by decompression, thick coronas with clinopyroxene suggest partial breakdown of amphibole because

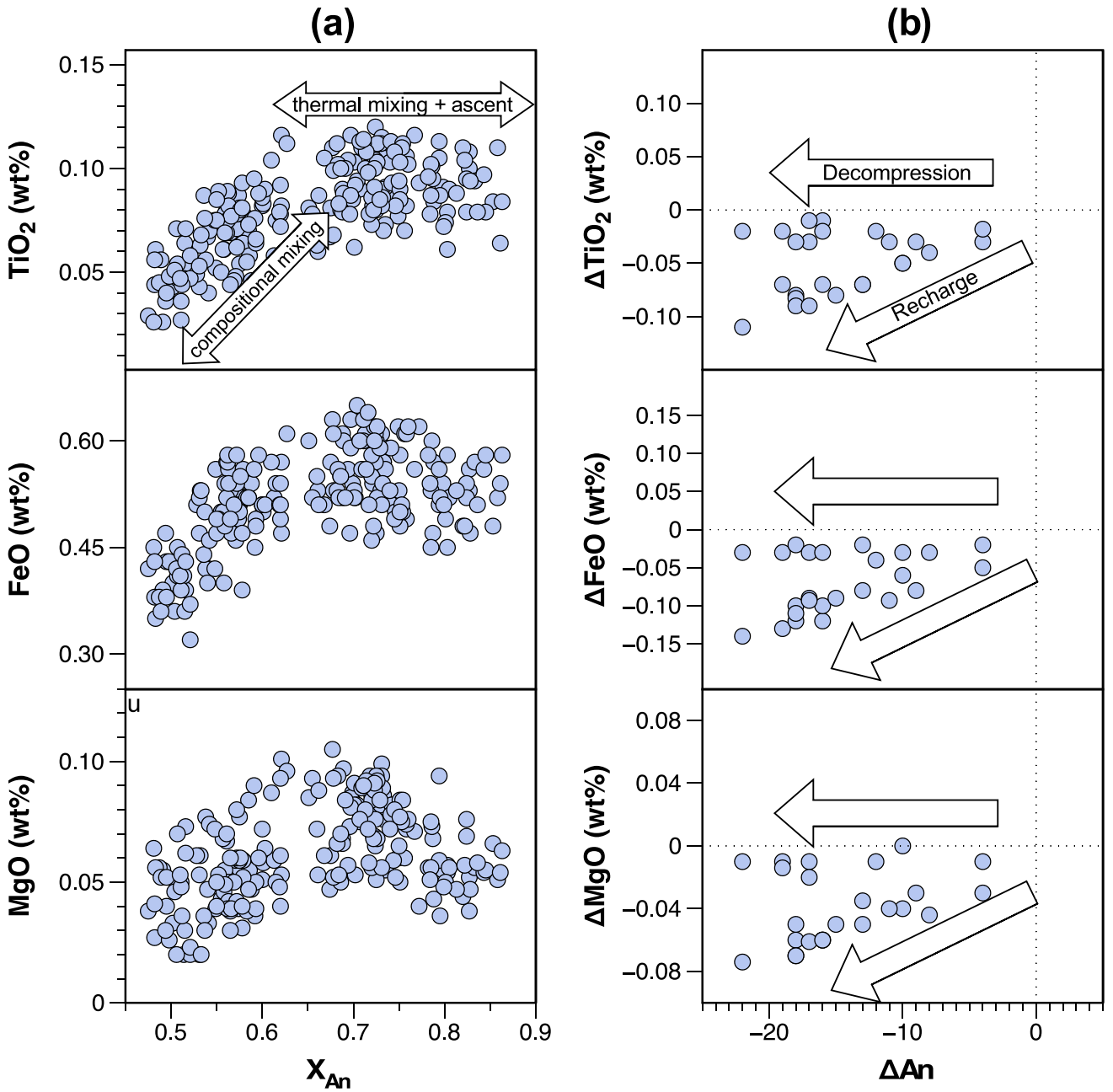

Fig. 8 **a** Variation of FeO, MgO and TiO_2 vs. X_{An} in plagioclase. Whilst the subhorizontal trend would indicate the dominance of closed-system behaviour with only heat transfer and decompression, the enrichment in Fe, Ti and Mg across resorption zones is interpreted to be related to a recharge magma event. **b** Relationships between ΔAn and ΔTiO_2, ΔFeO and ΔMgO through dusty zones in plagioclase (see comments in text)

of increasing magma temperature outside the amphibole stability field. (Rutherford and Devine 2003). Experimental data indicate that if amphibole is in contact with silicate melt under conditions outside its stability field, breakdown occurs within a few days. Accordingly, the presence of unrimmed amphiboles probably means that these amphiboles spent a very short time outside their field of stability during ascent (Rutherford and Hill 1993).

The occurrence of rhönite in close relationship with kaersutite may be the result of the destabilization of previously formed amphibole during the rise of the basaltic melt (Huckenholz and Kunzmann 1988). However, because the steep dP/dT slope of the stability curve for Ti-amphibole (Yagi et al. 1975; Merrill and Wyllie 1975; Huckenholz et al. 1992), particularly for pressures under 1500 MPa, the kaersutite breakdown to yield rhönite probably took place by

increase of temperature resulting from injection and flow of a new batch of melt rather than decompression. The fact that the reaction coronas are wrapped by plagioclase microlites of the groundmass would indicate that rhönite-bearing coronas were formed before crystallization of the groundmass. Furthermore, the absence of these coronas in a number of amphibole macrocrysts is consistent with the magma being outside the amphibole stability field for a short period of time before the eruption.

Geothermobarometric constraints

In addition to basic thermodynamic limitations, the large uncertainties in the petrological techniques used to estimate storage pressures make the Cpx-based barometry a delicate problem. Bulk-rock compositions may not necessarily represent primary melts and many assessments for equilibrium are unsuitable (Wieser et al. 2023a, b). Despite this, we have attempted to explore the depth of magma storage using the Cpx-only thermobarometer of Putirka (2008, 2016) since it is independent of temperature and H_2O content. The results show a wide range of pressures 340-830 MPa with a range of temperatures of 1060-1150 ºC (avg. 1090 ± 42 ºC), respectively. Applying the geothermometer of Faak et al. (2013) based on exchange of Mg between plagioclase and clinopyroxene yielded a temperature range of ≈ 1050-1130°C for $K(Pl/Cpx)^{Mg}$ = - 4.35 to - 4.45. The large range of pressures may be interpreted to represent polybaric storage, compositional differences and/or inherent uncertainty of the geobarometric model (Neave and Putirka 2017). Although there is a significant overlap and there are no clear differences between cores and rims, the lowest values correspond mostly to rims. Evidence in support of this is provided by the higher Ti/Al values for rims than for internal zones of the pyroxene macrocrysts (Fig. 5f).

Pressure estimates derived from the experimental calibration of hornblende geobarometer (Johnson et al 1989) yield a range of 700-815 MPa (avg. 770 ± 20 MPa). Although these authors carried out the experimental calibration with a phase assemblage different from that existing in the Armintza lava, nevertheless, these estimates are reasonably acceptable in light of experimental studies on the stability of Ti-rich amphiboles in alkaline basaltic lavas (Pilet et al. 2010). Kaersutite was found experimentally to be stable in association with clinopyroxene at pressures < 10 kbar and temperatures between 950 and 1050 ºC (Yagi et al. 1975), suggesting that it is stable not only in the lower crust but also in the upper mantle. Mantle-derived kaersutite seems to contain less Ti and more Al than kaersutite of crustal origin (Best 1974). However, although the kaersutite of this study has more Al than crustal kaersutites, its Ti content is slightly higher than that of mantle-derived kaersutites (Fig. 7d). Taking into account that ilmenite is ubiquitous in the basaltic rocks of Armintza, temperatures around 1080-1100 ºC for amphibole formation was calculated from data of Helz (1973) using the relation between Ti and temperature: T ºC = 273(Ti/23O) + 877 (Otten 1984). Temperatures based on amphibole compositions (Putirka 2016) are in a similar range (1060-1100 ºC). On the other hand, higher temperatures (1180-1210ºC) are obtained from the Ti content in calcium amphibole (Liao et al. 2021), even higher than those obtained from clinopyroxene.

An approximate calculation of magmatic water concentrations has been carried out using the plagioclase-liquid hygrometer-thermometer of Waters and Lange (2015) for plagioclases close to equilibrium (ΔAn ≈ 0) and temperatures in the range of 1050-1150 ºC, obtaining water contents between 1.76 and 2.25 wt% H_2O. We could also speculate on the redox state of the magma using the method of France et al. (2010) with the same plagioclases close to equilibrium, considering that for a moment they coexisted in equilibrium with pyroxenes in a liquid of similar composition to that of the bulk-rock, yielding values on the order of log fO_2 ≈ -7 to -8 corresponding to ΔFMQ +0.60-2.20.

Bearing in mind all these assessments, assuming a P-T range of ≈ 700-800 MPa and ≈ 1050-1150 ºC, respectively, for the pre-eruptive conditions of the basaltic magma, and using the approach and experimentally inferred equations of Popp et al. (1995, 2006), values of log fH_2 ≈ 1.15-1.44, log fH_2O ≈ 1.5-1.74 MPa and a_{H2O} ≈ 2.0 x 10^{-3} to 4.2 x 10^{-3} can be inferred from the average amphibole composition. These values correspond to melt H_2O contents of ≈ 0.42-0.70 wt% applying the H_2O-CO_2 solubility model of Allison et al. (eq. 8, 2022), which are less than the water estimates from the plagioclase-liquid hygrometer (≈ 2 wt%) with a log fH_2O ≈ 2.50-2.70, suggesting loss of H. Inasmuch as the partial pressure of H_2O is much lower than the estimated lithostatic pressure any fluid phase that occurs at the system will be lithostatically pressured (Spear 1993). This means that if the fluid is circumscribed to the H-O system, then the estimated H_2O activity would indicate either fluid-free crystallization conditions or that other components of the C-H-O system may be present, mainly CO_2. This is the second-most abundant fluid species in the Earth (Jambon 1994) and the estimated fugacity of O_2 (log fO_2 ≈ -8) is too oxidizing for graphite and CH_4 to be stable. Given the fH_2 and fH_2O inferred from kaersutite, CO_2 contents of ≈ 0.85 wt% are obtained or, in terms of fugacity, log fCO_2 ≈ 4.40-4.58, using the equations 6 and 10 of Iacovino et al. (2013). In comparison, with ≈ 2 % wt% H_2O we would have lower CO_2 contents and fugacities, ≈ 0.77-0.80 wt% and log fCO_2 ≈ 4.30-4.33, respectively. However, as Lamb and Popp (2009) claimed, these calculations do not denote that a free fluid phase was present, only that if $P_f = P_l$ the fluid is either rich in CO_2 or that there are other components in the system (e.g. sulphur).

Source and magma evolution

Mafic lavas associated with the Cretaceous alkaline magmatism of the Pyrenees were interpreted to be produced by fractionation of alkali basalts from mantle to lower-pressure crustal conditions (Azambre et al. 1992). The alkaline volcanism of the Basque-Cantabrian Basin probably represents a small-scale system in an extensional geodynamic environment. Its architecture was built as a result of a time-constrained series of eruptions of distinct magma batches within a time period spanning primarily from the Albian to the Santonian, as a result of melting of mantle sources. Recently, Pedrera et al. (2021) proposed a model for the magmatism in the Basque-Cantabrian Basin during Mesozoic times in which the asthenosphere rise and necking promoted the melting of the lithospheric mantle during rifting and hyperextension of the basin. According to these authors, the mantle sources were affected by OIB-type components perhaps produced by the ascending asthenosphere mantle during the later stages of rifting. The alkaline magmatism was ascribed to mixing between melt fractions of Grt-lherzolites and slightly higher melt contents of Sp-lherzolites, with possible contribution of Grt-pyroxenites. In this regard, the OIB-type alkaline basalts from the Errigoiti formation (Bizkaia) were attributed by Sarrionandia-Eguidazu et al. (2017) to low degrees of partial melting of a mantellic source containing garnet and spinel (40grt/60sp) at ≈ 70 km of depth, based on theoretical melting curves for the mantle defined by Jung et al (2006). Inasmuch as Dy/Yb and La/Yb values for the Armintza lava are in the ranges of 2.85-2.93 and 28.84-29.26, respectively, and plotting the composition of the lava on a plot of La/Yb vs. Dy/Yb (Fig. 13; Jung et al. 2006), it would represent a mixing of small-degree partial melts from garnet and spinel peridotite sources with a garnet/spinel ratio of ≈ 80/20. Additionally, based on values of the K/La and (Ce/Yb)N ratios and the model curves shown by Jung et al. (2006), the Armintza lava could be the result of 1-2% partial melting. It is possible that the Armintza lava flow forms part of the same magma plumbing system that the Errigoiti volcanism and other volcanic outcrops from the Biscay synclinorium.

However, a model including a simple mixing of melts derived from garnet and spinel peridotite sources is unable to simultaneously explain the petrological and geochemical constraints related to formation of alkaline basalts. The source of these rocks must be more enriched than the primitive mantle in terms of incompatible trace elements and must give rise to rocks with mostly constant Al_2O_3/TiO_2 and Na_2O/K_2O ratios (Pilet 2015). As this author states, the melting of amphibole-bearing metasomatic veins in the lithosphere is the key factor for the genesis of alkaline basalts in oceanic and continental settings. Experimental studies show that melting of metasomatised lithosphere containing amphibole-rich veins can reproduce the essential geochemical features of oceanic and continental alkaline magmas (Pilet et al. 2008). Amphiboles in mantle environments can be grouped into: (i) disseminated amphiboles in peridotite; and (ii) amphiboles related to hornblendite veins resulting from metasomatic processes in the lithospheric mantle (Ionov et al. 1997; Witt-Eickschen et al. 2003). Unlike the first one, amphiboles from metasomatic veins show concave downward REE patterns with maxima in Nd and relatively high Nb, Ta, Zr and Hf concentrations, with high Nb/Th and low Lu/Hf (6b, c). In fact, despite having slightly higher TiO_2 contents, the Al_2O_3/TiO_2 and Na_2O/K_2O ratios for the amphiboles in this study are within the compositional range observed in metasomatic vein amphiboles worldwide (Pilet 2015). Primitive mantle-normalised trace-element abundances for hypothetical melts in equilibrium with amphibole and pyroxene (Fig. 9) reveal a high degree of trace-element enrichment with a similar pattern to those corresponding to hornblendite and clinopyroxene hornblendite melts experimentally produced at 1.5 GPa (Pilet et al. 2008). Such experiments indicate that alkaline melts can be produced by melting of amphibole-bearing metasomatic veins within the lithosphere.

According to all these considerations, a model that could hypothetically account for the evolution of magma is illustrated in Fig. 10. A magma possibly entraining macrocrysts (antecrysts) from deeper levels of the mantle may have been ponded at depth (≈ -30 km), as evidenced from thermobarometry data. The steep trend showed on chondrite-normalized REE spectra compared to basalts from other tectonic settings (Fig. 2), and the lower Al_2O_3 contents relative to arcs at high MgO contents is evidence for a deeper origin for such melts (McGee and Smith 2016). Magma recharge and mixing with hotter, mafic magma and convective processes driven by new magma pulses led to the disaggregation of a mushy layer and intermingling of crystals with different thermal histories. These processes give rise to the juxtaposition of populations of plagioclase, clinopyroxene and amphibole macrocrysts with textures and compositions that reflect disequilibrium conditions. In addition, magma recharge combined with extensional tectonics is presumably the triggering event for the eruption. Recharge of new magma has been invoked as a process to trigger mixing and convection (Bergantz et al. 2015).

The occurrence of reverse zoning on the rims of dusty plagioclase and pyroxene macrocrysts indicates the close temporal relationship between mixing and eruption (Sakuyama 1984). Based on the rims of plagioclase are ≈ 20 to 60 µm wide, the time it took for the rim development prior to eruption is estimated to be around 5 days to 6 months using growth rates of ≈ 3 x 10^{-7} µm/s (Larsen 2005). Similar time scales stem from Mg diffusion using the relation $t = x^2/(4D^{Pl}_{Mg})$ where D^{Pl}_{Mg} is the diffusion coefficient for

Mg in plagioclase and x is the diffusional distance. With a D^{Pl}_{Mg} of 7.2 x 10^{-4} $\mu m^2/s$ (Van Orman et al. 2014), for ≈ An75 and a temperature for the lava of ≈ 1100ºC we obtain a time lag between rim formation and eruption on the order of ≈ 15 days to 5 months. Timescales calculated at the same conditions using a diffusion coefficient D^{Pl}_{Mg} = 5.2 x 10^{-8} $\mu m^2/s$ (Faak et al. 2013), which explicitly buffer a_{SiO2} in their experiments, are on the order of 20 days and 7 months. These values are similar to those based on crystal growth rate. Clinopyroxene growth rates have been estimated empirically and experimentally converging on the order of 10^{-4} to 10^{-5} μms^{-1} for low to high undercoolings, respectively (Orlando et al. 2008). According to this growth rate, rims of ≈ 80 µm thick are inferred to have formed over 9 days to 3 months, reflecting the time elapsed between recharge and eruption. Given that most mafic phases take more than a year to completely homogenize chemical heterogeneities (Gerlach and Grove 1982), eruption should occur within one year after the recharge and mixing to maintain the reverse-zoned rims as a result of these processes. Anyway, several factors can account for the timescale variability and discrepancies, e.g., different experimental conditions, diffusional anisotropy, improper fitting, uncertaintites in partitioning models, or even to underlying magmatic processes (Mutch et al. 2021).

Quantitative studies of magma ascent rates reveal that intraplate alkaline basalts rise from near-source mantle depths, where some storage can occur, and ascend rapidly through the crust (Brenna et al. 2021). Consequently, because the extent to which primary magmas change in composition is related to the rate of magma ascent, fractionation and assimilation are not expected to significantly modify the chemical characteristics of alkaline basalts, particularly those related with small volume eruptions (McGee and Smith 2016). This would account for the fact that alkaline submarine volcanism of the Basque-Cantabrian basin is mainly represented by basalts with minor trachyte to trachyandesite occurrences. Given that the ΔAn (%Ancore-%Anrim) across resorption surfaces varies from - 3 to - 22 (Fig. 8b), the magma would have experienced a decompression of about ≈ 25 km assuming a change in plagioclase composition as a function of pressure of ≈ 3% An/kb (Ustunisik et al. 2014). This is consistent with the geobarometric data and the large distance over which decompression occurred is in agreement with estimates of crustal thickness during the Albian (≈ 20-30 km, Pedrera et al. 2021).

A basaltic magma containing ≈ 2.0 wt% H_2O rising through continental crust in subaerial settings is H_2O saturated at confining pressures of about 40 MPa, which is equivalent to ≈ 1.6 km considering a typical continental lithostatic pressure gradient of 24.5-25 $MPakm^{-1}$ (Wallace et al. 2015; Cas and Simmons 2018). However, taking into account the effect of hydrostatic pressure on the saturation of volatiles, for an estimated water depth of around 500 m (López-Horgue com. pers.) and applying equation 2 of Cas and Simmons (2018), the basaltic magma with ≈ 2 wt% dissolved H_2O will have reached saturation in water at crustal pressures of 35 MPa, equivalent to a submarine crustal depth of ≈ 1.4 km. Due to relative difference between H_2O and CO_2 solubilities, and based on saturation models of Dixon (1997), the basaltic melt of

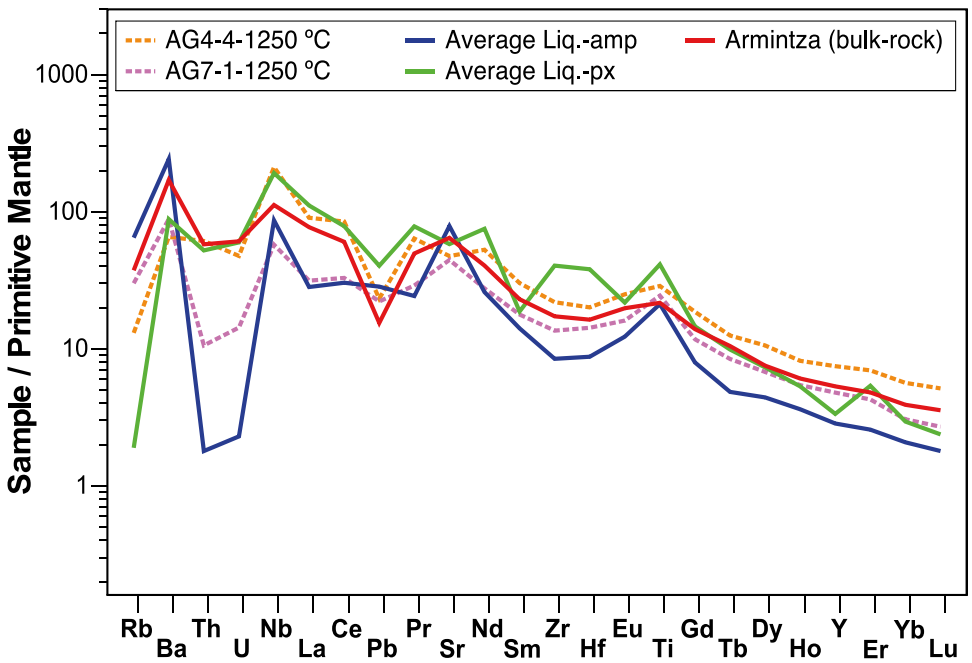

Fig. 9 Trace element pattern of the Armintza lava compared with the hypothetical melts in equilibrium with amphibole and pyroxene and the primitive mantle-normalised trace-element concentrations for hornblendite (AG-4) and clinopyroxene-hornblendite (AG-7) melts (Pilet et al. 2008). Trace element partition coefficients between clinopyroxene, amphibole and alkali basaltic melt from Bonechi et al. (2021, 2023)

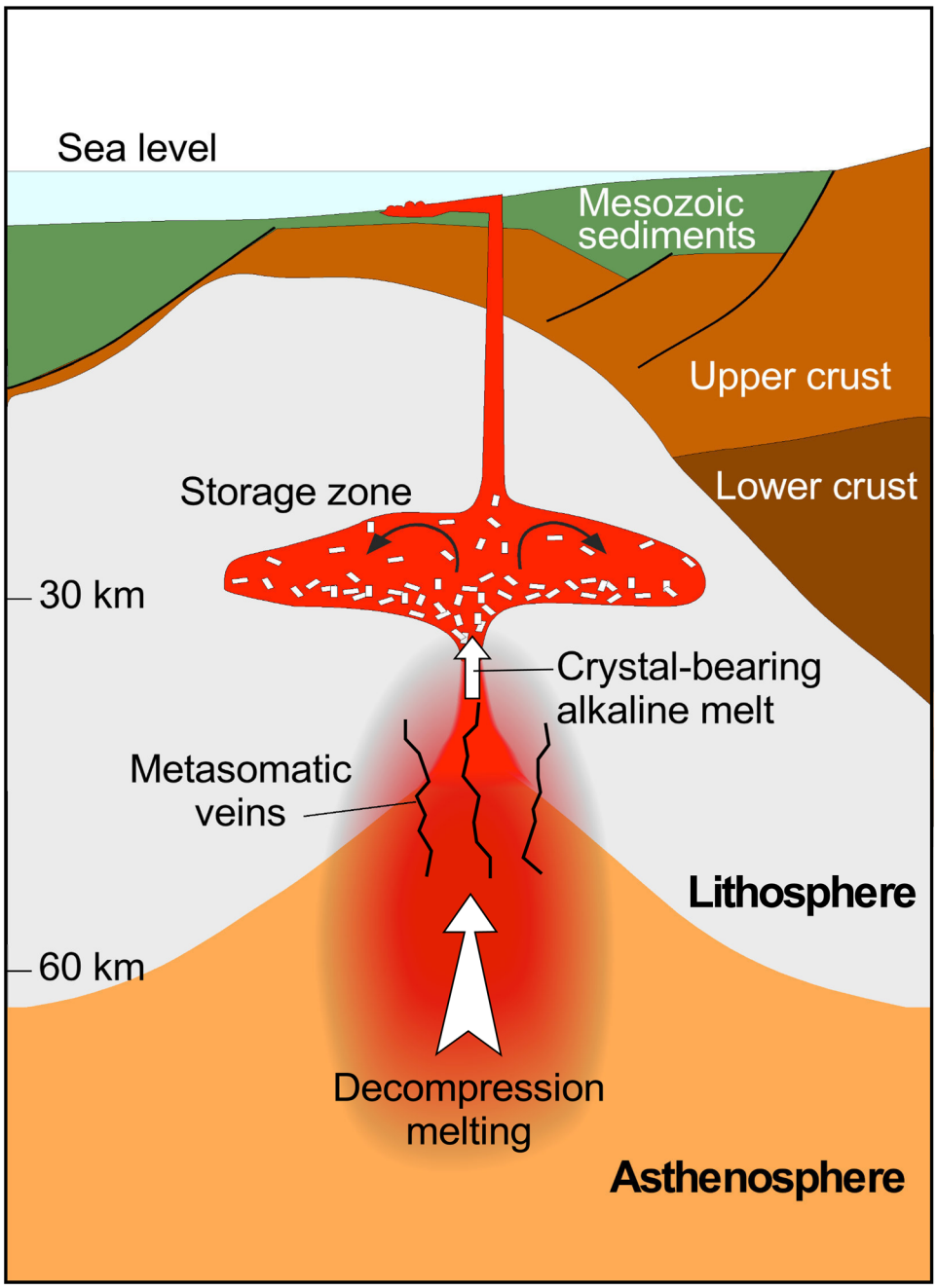

Fig. 10 Schematic diagram showing the proposed model for the formation of alkaline lavas based on the models of Pilet (2015) and Pedrera et al. (2021). Decompression melting in the asthenosphere mantle yielded low degree melts that percolate through the lithosphere. This process gives rise to a metasomatic zone with amphibole-bearing veins to produce alkaline melts. These ascend to a storage zone in the lithospheric mantle where crystallization, mixing and convective processes occur

this study with $CO_2/H_2O \approx 0.3$-0.4 became saturated in CO_2 and began degassing at about 300 MPa. In addition, under the H_2O saturation conditions, and based on volatile saturation curves for CO_2 (Wallace et al. 2015; Cas and Simmons 2018), maximum CO_2 contents of the order of 100 ppm can be expected, which would mean a significant loss of CO_2 during magmatic rise.

Conclusions

This paper deals with a pillow lava interbedded with Upper Albian-Lower Cenomanian sediments that occurs in the Basque-Cantabrian Basin (Armintza, Bizkaia, N Spain). The pillow lava is a porphyritic aphanitic basalt of alkaline nature with abundant macrocrysts of clinopyroxene,

Ca-rich plagioclase (50-86 mol%), kaersutite and ilmenite. The groundmass consists mainly of microlites of plagioclase, very fine-grained clinopyroxene, ilmenite, rhönite in close association with kaersutite, apatite and Fe sulphides. The pillow lava has a relatively homogeneous bulk-rock composition and enrichment of incompatible trace elements, with REE patterns, Al_2O_3/TiO_2 (3.38-3.41) and Na_2O/K_2O (2.59-3.49) ratios typical of OIB-type or intraplate basalts.

Mineral textures and compositions reveal a complex magmatic history involving open-system magmatic processes such as recharge and mixing. Analysis of compositional zoning in macrocrysts suggests time intervals on short time scales (days to months) between magma recharge and eruption. Overall, pressures and temperatures of ≈ 700-800 MPa and ≈ 1050-1150 ºC, respectively, are estimated for the pre-eruptive conditions by using clinopyroxene, plagioclase and amphibole in combination as thermobarometers.

Trace element compositions of clinopyroxenes and amphiboles determined by LA-ICP-MS are consistent with those from clinopyroxenite and hornblendite magmatic veins. Hypothetical melts in equilibrium with pyroxenes and amphiboles show trace-element patterns similar to alkaline melts produced experimentally from amphibole-bearing metasomatic veins within the lithosphere, which overlap in their patterns with those of the Armintza basaltic lava. Accordingly, a metasomatised lithospheric mantle including amphibole-rich veins is interpreted as the most likely source for the alkaline basaltic melt.

The alkaline volcanism of the Basque-Cantabrian Basin constitutes a small-scale system in an extensional geodynamic environment, which was built during a series of time-limited eruptions of different batches of magma that took place mainly from the Albian to the Santonian. Inasmuch as minerals as plagioclase, ferromagnesian silicates and Fe-Ti oxides are sensitive to changing magmatic conditions through their textures and compositional variations, it would also be interesting to focus attention on mineral phases from others volcanic outcrops to better understand the Cretaceous magmatism of the Basque-Cantabrian Basin.

Supplementary Information The online version contains supplementary material available at https://doi.org/10.1007/s00710-024-00850-9.

Acknowledgements The authors are grateful to Pilar Montero for assistance with LA-ICP analyses. We also thank Juan Manuel Gutiérrez Zorrilla for his comments on fugacities of volatile components at high pressures and temperatures. We thank the University of the Basque Country for the financial support. The comments and suggestions of Dr. Ömer Kamacı and an anonymous reviewer are greatly appreciated. We further thank the editor Chao Wang for his insightful comments that helped improve the manuscript.

Funding Open Access funding provided thanks to the CRUE-CSIC agreement with Springer Nature.

References

Allison CM, Roggensack K, Clarke AB (2022) MafiCH: a general model for H_2O–CO_2 solubility in mafic magmas. Contrib Mineral Petrol 177:40. https://doi.org/10.1007/s00410-022-01903-y

Azambre B, Rossy M, Albarede F (1992) Petrology of the alkaline magmatism from the Cretaceous North-Pyrenean rift zone (France and Spain). Eur J Mineral 4(4):813–834. https://doi.org/10.1127/ejm/4/4/0813

Bédard JH (2006) Trace element partitioning in plagioclase feldspar. Geochim Cosmochim Acta 70(14):3717–3742. https://doi.org/10.1016/j.gca.2006.05.003

Bennett EN, Lissenberg CJ, Cashman KV (2019) The significance of plagioclase textures in mid-ocean ridge basalt (Gakkel Ridge, Arctic Ocean). Contrib Mineral Petrol 174(6):49. https://doi.org/10.1007/s00410-019-1587-1

Bergantz GW, Schleicher JM, Burgisser A (2015) Open-system dynamics and mixing in magma mushes. Nat Geosci 8(10):793–796. https://doi.org/10.1038/ngeo2534

Best MG (1974) Mantle-derived amphibole within inclusions in alkalic-basaltic lavas. J Geophys Res 79(14):2107–2113. https://doi.org/10.1029/JB079i014p02107

Bindeman IN, Davis AM (2000) Trace element partitioning between plagioclase and melt: investigation of dopant influence on partition behavior. Geochim Cosmochim Acta 64(16):2863–2878. https://doi.org/10.1016/S0016-7037(00)00389-6

Bindeman IN, Davis AM, Drake MJ (1998) Ion microprobe study of plagioclase-basalt partition experiments at natural concentration levels of trace elements. Geochim Cosmochim Acta 62(7):1175–1193. https://doi.org/10.1016/S0016-7037(98)00047-7

Blundy J, Cashman K, Humphreys M (2006) Magma heating by decompression-driven crystallization beneath andesite volcanoes. Nature 443(7107):76–80. https://doi.org/10.1038/nature05100

Bonaccorsi E, Merlino S, Pasero M (1990) Rhonite - structural and microstructural features, crystal-chemistry and polysomatic relationships. Eur J Mineral 2(2):203–218

Bonechi B, Fabbrizio A, Perinelli C, Gaeta M, Petrelli M (2023) Experimental investigation of trace element partitioning between amphibole and alkali basaltic melt: Toward a more general partitioning model with implications for amphibole fractionation at deep crustal levels. Am Mineral 108(9):1678–1691. https://doi.org/10.2138/am-2022-8536

Bonechi B, Perinelli C, Gaeta M, Fabbrizio A, Petrelli M, Strnad L (2021) High pressure trace element partitioning between clinopyroxene and alkali basaltic melts. Geochim Cosmochim Acta 305:282–305. https://doi.org/10.1016/j.gca.2021.04.023

Brenna M, Ubide T, Nichols ARL, Mollo S, Pontesilli A (2021) Anatomy of Intraplate Monogenetic Alkaline Basaltic Magmatism: Clues From Magma, Crystals, and Glass. In: Masotta M, Beier C, and Mollo S (ed) Crustal Magmatic System Evolution: Anatomy, Architecture, and Physico-Chemical Processes. AGU Geophysical Monograph pp 79–103

Cao G, Xue H, Tong Y (2022) Complex magmatic processes recorded by clinopyroxene phenocrysts in a magmatic plumbing system: A case study of mafic volcanic rocks from the Laiyang Basin, southeastern North China Craton. Lithos 416–417:106673. https://doi.org/10.1016/j.lithos.2022.106673

Carracedo M, Larrea FJ, Alonso A (1999) Estructura y organizacion de las coladas submarinas: Caracteristicas de las lavas almohadilladas de edad cretacica que afloran en la Cordillera Vasco-Cantabrica. Estud Geol 55:209–222. https://doi.org/10.3989/egeol.99555-6161

Carracedo Sánchez M, Sarrionaindia F, Juteau T, Gil Ibarguchi JI (2012) Structure and organization of submarine basaltic flows: sheet flow transformation into pillow lavas in shallow submarine environments. Int J Earth Sci 101:2201–2214. https://doi.org/10.1007/s00531-012-0783-2

Cas RAF, Simmons JM (2018) Why deep-water eruptions are so different from subaerial eruptions. Front Earth Sci 6:198. https://doi.org/10.3389/feart.2018.00198

Cashman KV, Sparks RS, Blundy JD (2017) Vertically extensive and unstable magmatic systems: a unified view of igneous processes. Science 355(6331):eaag3055. https://doi.org/10.1126/science.aag3055

Castañares LM, Robles S (2004) El vulcanismo del albiense-santoniense en la cuenca vasco-cantábrica. In: Vera JA (ed) Geología de España. SGE-IGME, Madrid, pp 306–308

Castañares LM, Robles S, Gimeno D, Bravo JCV (2001) The submarine volcanic system of the Errigoiti Formation (Albian-Santonian of the Basque-Cantabrian basin, northern Spain): Stratigraphic framework, facies, and sequences. J Sediment Res 71(2):318–333. https://doi.org/10.1306/080700710318

Castañares LM, Robles S, Vicente-Bravo JC (1997) Distribución estratigráfica de los episodios volcánicos submarinos del Albiense-Santoniense en la Cuenca Vasca (sector Gernika-Pientzia, Bizkaia). Geogaceta 22:43–46

Coote A, Shane P (2018) Open-system magmatic behaviour beneath monogenetic volcanoes revealed by the geochemistry, texture and thermobarometry of clinopyroxene, Kaikohe-Bay of Islands volcanic field (New Zealand). J Volcanol Geotherm Res 368:51–62. https://doi.org/10.1016/j.jvolgeores.2018.11.006

Couch S, Sparks RS, Carroll MR (2001) Mineral disequilibrium in lavas explained by convective self-mixing in open magma chambers. Nature 411(6841):1037–1039. https://doi.org/10.1038/35082540

De Jongh WK (1973) X-ray fluorescence analysis applying theoretical matrix corrections. Stainless steel. X-Ray Spectrom 2(4):151–158. https://doi.org/10.1002/xrs.1300020404

Deer WA, Howie RA, Zussman J (2013) An introduction to the rock-forming minerals (3rd Edition). Mineralogical Society of Great Britain and Ireland, 498 pp

Dixon JE (1997) Degassing of alkalic basalts. Am Mineral 82(3–4):368–378. https://doi.org/10.2138/am-1997-3-415

Dohmen R, Blundy J (2014) A predictive thermodynamic model for element partitioning between plagioclase and melt as a function of pressure, temperature and composition. Am J Sci 314(9):1319–1372. https://doi.org/10.2475/09.2014.04

Edmonds M, Cashman KV, Holness M, Jackson M (2019) Architecture and dynamics of magma reservoirs. Philos Trans A Math Phys Eng Sci 377(2139):20180298. https://doi.org/10.1098/rsta.2018.0298

Erdmann S, Martel C, Pichavant M, Kushnir A (2014) Amphibole as an archivist of magmatic crystallization conditions: problems, potential, and implications for inferring magma storage prior to the paroxysmal 2010 eruption of Mount Merapi, Indonesia. Contrib Mineral Petrol 167:1016. https://doi.org/10.1007/s00410-014-1016-4

Faak K, Chakraborty S, Coogan LA (2013) Mg in plagioclase: Experimental calibration of a new geothermometer and diffusion coefficients. Geochim Cosmochim Acta 123:195–217. https://doi.org/10.1016/j.gca.2013.05.009

France L, Ildefonse B, Koepke J, Bech F (2010) A new method to estimate the oxidation state of basaltic series from microprobe analyses. J Volcanol Geotherm Res 189(3–4):340–346. https://doi.org/10.1016/j.jvolgeores.2009.11.023

García-Garmilla F, Carracedo Sánchez M (1989) Diagenetic processes in the Ibarretxe Member (Lower Cretaceous, Bilbao, northern Spain). Kobie 18:51–61

García-Mondéjar J, Carracedo-Sánchez M, Owen HG, Fernández-Mendiola PA, Somerville ID (2018) The Early Aptian volcanic episode of Gutiolo (N Spain): expression of the Bilbao Rift Fault Zone. Geol J. https://doi.org/10.1002/gj.3342

Gerlach DC, Grove TL (1982) Petrology of Medicine Lake Highland volcanics: characterization of endmembers of magma mixing. Contrib Mineral Petrol 80(2):147–159. https://doi.org/10.1007/BF00374892

Ginibre C, Wörner G, Kronz A (2002) Minor- and trace-element zoning in plagioclase: implications for magma chamber processes at Parinacota volcano, northern Chile. Contrib Mineral Petrol 143(3):300–315. https://doi.org/10.1007/s00410-002-0351-z

Giuliani L, Iezzi G, Vetere F, Behrens H, Mollo S, Cauti F, Ventura G, Scarlato P (2020) Evolution of textures, crystal size distributions and growth rates of plagioclase, clinopyroxene and spinel crystallized at variable cooling rates from a mid-ocean ridge basaltic melt. Earth-Science Rev 204:103165. https://doi.org/10.1016/j.earscirev.2020.103165

Govindaraju K (1994) 1994 compilation of working values and sample description for 383 geostandards. Geostand Newslett 18:1–158. https://doi.org/10.1046/j.1365-2494.1998.53202081.x-i1

Grapes RH, Wysoczanski RJ, Hoskin PWO (2003) Rhonite paragenesis in pyroxenite xenoliths, Mount Sidley volcano, Marie Byrd Land. West Antarctica. Mineral Mag 67(4):639–651. https://doi.org/10.1180/0026461036740123

Grew ES, Hålenius U, Pasero M, Barbier J (2008) Recommended nomenclature for the sapphirine and surinamite groups (sapphirine supergroup). Mineral Mag 72(4):839–876. https://doi.org/10.1180/minmag.2008.072.4.839

Hawthorne F, Oberti R, Harlow G, Maresch W, Martin RF, Schumacher J, Welch M (2012) IMA report: nomenclature of the amphibole supergroup. Am Mineral 97:2031–2048. https://doi.org/10.2138/am.2012.4276

Hawthorne FC, Oberti R, Zanetti A, Czamanske GK (1998) The role of Ti in hydrogen-deficient amphiboles; sodic-calcic and sodic amphiboles from Coyote Peak. California. Can Mineral 36(5):1253–1265

Helz RT (1973) Phase relations of basalts in their melting range at PH2O = 5 kb as a function of oxygen fugacity1: Part I. mafic phases. J Petrol 14(2):249–302. https://doi.org/10.1093/petrology/14.2.249

Holness MB, Stock MJ, Geist D (2019) Magma chambers versus mush zones: constraining the architecture of sub-volcanic plumbing systems from microstructural analysis of crystalline enclaves. Philos Trans A Math Phys Eng Sci 377(2139):20180006. https://doi.org/10.1098/rsta.2018.0006

Huckenholz HG, Gilbert MC, Kunzmann T (1992) Stability and phase relations of calcic amphiboles crystallized from magnesio-hastingsite compositions in the 1 to 45 kbar pressure range. N Jahr Miner Abh 164:229–268

Huckenholz HG, Kunzmann T (1988) Occurrence, formation and stability of rhoenite in Hocheifel tertiary alkali basalt. Fortschr Mineral 66:71–71

Hutchison CS (1974) Laboratory handbook of petrographic techniques. Wiley-Interscience, New York, p 527

Iacovino K, Moore GM, Roggensack K, Oppenheimer C, Kyle PR (2013) H_2O-CO_2 solubility in mafic alkaline magma: applications to volatile sources and degassing behavior at Erebus volcano, Antarctica. Contrib Mineral Petrol 166:845–860. https://doi.org/10.1007/s00410-013-0877-2

Ionov DA, Griffin WL, O'Reilly SY (1997) Volatile-bearing minerals and lithophile trace elements in the upper mantle. Chem Geol 141(3):153–184. https://doi.org/10.1016/S0009-2541(97)00061-2

Ionov DA, Hofmann AW (1995) Nb-Ta-rich mantle amphiboles and micas: implications for subduction-related metasomatic trace element fractionations. Earth Planet Sci Lett 131(3):341–356. https://doi.org/10.1016/0012-821X(95)00037-D

Jambon A (1994) Earth degassing and large-scale geochemical cycling of volatile elements. In: Carroll MR, and Holloway JR (ed) Volatiles in Magmas. Rev Mineral Mineral Soc Am 30:479–518

Jerram DA, Dobson KJ, Morgan DJ, Pankhurst MJ (2018) The petrogenesis of magmatic systems: using igneous textures to understand magmatic processes. In: Burchardt S (ed) Volcanic and Igneous Plumbing Systems. Elsevier, pp 191–229

Johnson M, Rutherford M, Hess P (1989) Experimental study of igneous kaersutite stability with application to snc petrogenesis. Abstracts of the Lunar and Planetary Science Conference 20:472

Jung C, Jung S, Hoffer E, Berndt J (2006) Petrogenesis of tertiary mafic alkaline magmas in the hocheifel Germany. J Petrol 47(8):1637–1671. https://doi.org/10.1093/petrology/egl023

Kamacı Ö, Altunkaynak Ş (2019) Magma chamber processes and dynamics beneath northwestern Anatolia: Insights from mineral chemistry and crystal size distributions (CSDs) of the Kepsut volcanic complex (NW Turkey). J Asian Earth Sci 181:103889. https://doi.org/10.1016/j.jseaes.2019.103889

Kong F-M, Schertl H-P, Zhao L-Q, Li X-P, Liu X-H (2020) Rhönite in Cenozoic alkali basalt from Changle, Shandong Province, China, and its significance. Eur J Mineral 32(3):325–346. https://doi.org/10.5194/ejm-32-325-2020

Kunzmann T (1999) The aenigmatite-rhonite mineral group. Eur J Mineral 11(4):743–756

Lamb W, Popp R (2009) Amphibole equilibria in mantle rocks: Determining values of mantle aH_2O and implications for mantle H2O contents. Am Mineral 94:41–52. https://doi.org/10.2138/Am.2009.2950

Lamolda MA, Mathey B, Rossy M, Sigal J (1983) La edad del volcanismo cretácico de Vizcaya y Guipúzcoa. Estud Geol 39:151–155

Larsen JF (2005) Experimental study of plagioclase rim growth around anorthite seed crystals in rhyodacitic melt. Am Mineral 90(2–3):417–427. https://doi.org/10.2138/am.2005.1456

LaTourrette T, Hervig RL, Holloway JR (1995) Trace element partitioning between amphibole, phlogopite, and basanite melt. Earth Planet Sci Lett 135(1):13–30. https://doi.org/10.1016/0012-821X(95)00146-4

Le Bas MJ (1962) The role of aluminum in igneous clinopyroxenes with relation to their parentage. Am J Sci 260(4):267–288. https://doi.org/10.2475/ajs.260.4.267

Liao Y, Wei C, Rehman HU (2021) Titanium in calcium amphibole: Behavior and thermometry. Am Mineral 106(2):180–191. https://doi.org/10.2138/am-2020-7409

Mangler MF, Humphreys MCS, Wadsworth FB, Iveson AA, Higgins MD (2022) Variation of plagioclase shape with size in intermediate magmas: a window into incipient plagioclase crystallisation. Contrib Mineral Petrol 177(64). https://doi.org/10.1007/s00410-022-01922-9

McDonough W, Sun SS (1995) The composition of the Earth. Chem Geol 67:1050–1056. https://doi.org/10.1016/0009-2541(94)00140-4

McGee LE, Smith IEM (2016) Interpreting chemical compositions of small scale basaltic systems: A review. J Volcanol Geotherm Res 325:45–60. https://doi.org/10.1016/j.jvolgeores.2016.06.007

Merrill RB, Wyllie PJ (1975) Kaersutite and Kaersutite Eclogite from Kakanui, New Zealand — Water-Excess and Water-Deficient Melting to 30 Kilobars. GSA Bulletin 86(4):555–570. https://doi.org/10.1130/0016-7606(1975)86%3c555:Kakefk%3e2.0.Co;2

Miró J, Manatschal G, Cadenas P, Muñoz JA (2021) Reactivation of a hyperextended rift system: the Basque-Cantabrian Pyrenees case. Basin Res 33(6):3077–3101. https://doi.org/10.1111/bre.12595

Molendijk SM, Buchs DM, Mason PRD, Blundy JD (2022) Clinopyroxene diversity and magma plumbing system processes in an accreted Pacific ocean island, Panama. Contrib Mineral Petrol 177(30). https://doi.org/10.1007/s00410-022-01894-w

Mollo S, Hammer J (2017) Dynamic crystallization in magmas. In: Heinrich W, and Abart R (ed) 16, Mineral reaction kinetics: Microstructures, textures, chemical and isotopic signatures. European Mineralogical Union Notes in Mineralogy, vol. 16, pp 378–418

Mollo S, Putirka K, Misiti V, Soligo M, Scarlato P (2013) A new test for equilibrium based on clinopyroxene–melt pairs: Clues on the solidification temperatures of Etnean alkaline melts at post-eruptive conditions. Chem Geol 352:92–100. https://doi.org/10.1016/j.chemgeo.2013.05.026

Montigny R, Azambre B, Rossy M, Thuizat R (1986) K-Ar study of cretaceous mag- matism and metamorphism in the Pyrenees : age and length of rotation of the Iberian Peninsula. Tectonophysics 129:257–273. https://doi.org/10.1016/0040-1951(86)90255-6

Morimoto N, Fabries J, Ferguson AK, Ginzburg IV, Ross M, Seifert FA, Zussman J, Aoki K, Gottardi G (1988) Nomenclature of Pyroxenes. Am Mineral 73:1123–1133

Mutch EJF, Maclennan J, Shorttle O, Rudge JF, Neave DA (2021) DFENS: diffusion chronometry using finite elements and nested sampling. Geochem Geophys Geosyst 22(4):e2020GC009303. https://doi.org/10.1029/2020gc009303

Nakamura M, Shimakita S (1998) Dissolution origin and syn-entrapment compositional change of melt inclusion in plagioclase. Earth Planet Sci Lett 161(1):119–133. https://doi.org/10.1016/S0012-821X(98)00144-7

Neave DA, Putirka KD (2017) A new clinopyroxene-liquid barometer, and implications for magma storage pressures under Icelandic rift zones. Am Mineral 102(4):777–794. https://doi.org/10.2138/am-2017-5968

Nelson ST, Montana A (1992) Sieve-textured plagioclase in volcanic rocks produced by rapid decompression. Am Mineral 77(11–12):1242–1249

Nisbet EG, Pearce JA (1977) Clinopyroxene composition in mafic lavas from different tectonic settings. Contrib Mineral Petrol 63(2):149–160. https://doi.org/10.1007/BF00398776

Orlando A, D'Orazio M, Armienti P, Borrini D (2008) Experimental determination of plagioclase and clinopyroxene crystal growth rates in an anhydrous trachybasalt from Mt Etna (Italy). Eur J Mineral 20(4):653–664. https://doi.org/10.1127/0935-1221/2008/0020-1841

Otten MT (1984) The origin of brown hornblende in the Artfjället gabbro and dolerites. Contrib Mineral Petrol 86:189–199. https://doi.org/10.1007/BF00381846

Pearce JA (2008) Geochemical fingerprinting of oceanic basalts with applications to ophiolite classification and the search for Archean oceanic crust. Lithos 100(1–4):14–48. https://doi.org/10.1016/j.lithos.2007.06.016

Pearce TH, Kolisnik AM (1990) Observations of plagioclase zoning using interference imaging. Earth Sci Rev 29(1):9–26. https://doi.org/10.1016/0012-8252(0)90024-P

Pe-Piper G (1984) Zoned pyroxenes from shoshonite lavas of Lesbos, Greece: inferences concerning shoshonite petrogenesis. J

Petrol 25(2):453–472. https://doi.org/10.1093/petrology/25.2.453

Pedrera A, García-Senz J, Ayala C, Ruiz-Constán A, Rodríguez-Fernández LR, Robador A, González Menéndez L (2017) Reconstruction of the exhumed mantle across the north iberian margin by crustal-scale 3-D gravity inversion and geological cross section. Tectonics 36(12):3155–3177. https://doi.org/10.1002/2017tc004716

Pedrera A, García-Senz J, Peropadre C, Robador A, López-Mir B, Díaz-Alvarado J, Rodríguez-Fernández LR (2021) The Getxo crustal-scale cross-section: testing tectonic models in the Bay of Biscay-Pyrenean rift system. Earth Sci Rev 212:103429. https://doi.org/10.1016/j.earscirev.2020.103429

Pilet S (2015) Generation of low-silica alkaline lavas: Petrological constraints, models, and thermal implications. In: Foulger GR, Lustrino M, and King SD(ed). The Interdisciplinary Earth: A Volume in Honor of Don L. Anderson. Geological Society of America, pp 281–304

Pilet S, Baker MB, Stolper EM (2008) Metasomatized Lithosphere and the Origin of Alkaline Lavas. Science 320(5878):916–919. https://doi.org/10.1126/science.1156563

Pilet S, Ulmer P, Villiger S (2010) Liquid line of descent of a basanitic liquid at 1.5 Gpa: constraints on the formation of metasomatic veins. Contrib Mineral Petrol 159(5):621–643. https://doi.org/10.1007/s00410-009-0445-y

Popp R, Virgo D, Yoder HS, Hoering TC, Phillips MW (1995) An experimental study of phase equilibria and Fe oxy-component in kaersutitic amphibole: implications for the fH_2 and aH_2O in the upper mantle. Am Mineral 80:534–548. https://doi.org/10.2138/am-1995-5-614

Popp RK, Hibbert HA, Lamb WM (2006) Oxy-amphibole equilibria in Ti-bearing calcic amphiboles: experimental investigation and petrologic implications for mantle-derived amphiboles. Am Mineral 91(1):54–66. https://doi.org/10.2138/am.2006.1838

Pouchou JL, Pichoir F (1985) "PAP" φ(ρZ) procedure for improved quantitative microanalysis. In: Armstrong JT (ed) Microbean Analysis. San Francisco Press, San Francisco, California, pp 104–106

Powell W, Zhang M, O'Reilly SY, Tiepolo M (2004) Mantle amphibole trace-element and isotopic signatures trace multiple metasomatic episodes in lithospheric mantle, western Victoria, Australia. Lithos 75(1–2):141–171

Putirka KD (2008) Thermometers and barometers for volcanic systems. In: Putirka KD, and Tepley III FJ (ed) Minerals, Inclusions and Volcanic Processes, vol 69, Rev Mineral Geochem. Mineral Soc Am-Geochem Soc, pp 61–120

Putirka KD (2016) Amphibole thermometers and barometers for igneous systems and some implications for eruption mechanisms of felsic magmas at arc volcanoes. Am Mineral 101(4):841–858. https://doi.org/10.2138/am-2016-5506

Robles S (2014) Evolución geológica de la Cuenca Vasco-Cantábrica. In: Bodego A, Mendia M, Aranburu A, Apraiz A (eds) Geología de la Cuenca Vasco-Cantábrica. Servicio editorial de la Universidad del País Vasco (UPV/EHU), Bilbao, pp 9–103

Rossy M, Azambre B, Albarède F (1992) REE and Sr/1bNd isotope geochemistry of the alkaline magmatism from the Cretaceous North Pyrenean Rift Zone (France-Spain). Chem Geol 97(1):33–46. https://doi.org/10.1016/0009-2541(92)90134-Q

Ruprecht P, Wörner G (2007) Variable regimes in magma systems documented in plagioclase zoning patterns: El Misti stratovolcano and Andahua monogenetic cones. J Volcanol Geotherm Res 165(3–4):142–162. https://doi.org/10.1016/j.jvolgeores.2007.06.002

Rutherford MJ, Devine JD (2003) Magmatic conditions and magma ascent as indicated by hornblende phase equilibria and reactions in the 1995–2002 Soufrière Hills Magma. J Petrol 44:1433–1453. https://doi.org/10.1093/petrology/44.8.1433

Rutherford MJ, Hill PM (1993) Magma ascent rates from amphibole breakdown: an experimental study applied to the 1980–1986 Mount St. Helens eruptions. J Geophys Res [Solid Earth] 98(B11):19667–19685. https://doi.org/10.1029/93jb01613

Sakuyama M (1984) Magma mixing and magma plumbing systems in island arcs. Bulletin Volcanologique 47(4):685–703. https://doi.org/10.1007/BF01952339

Sarrionandia Eguidazu F, Carracedo Sánchez M, Errandonea-Martin J, Eguiluz Alarcón L (2017) Petrogenesis of the alkali dikes of Errigoiti (Upper Cretaceous magmamtism in the Basque-Cantabrian Basin). Geogaceta 61:107–110

Shane P, Smith VC (2013) Using amphibole crystals to reconstruct magma storage temperatures and pressures for the post-caldera collapse volcanism at Okataina volcano. Lithos 156-159:159–170. https://doi.org/10.1016/j.lithos.2012.11.008

Shea T, Hammer JE (2013) Kinetics of cooling- and decompression-induced crystallization in hydrous mafic-intermediate magmas. J Volcanol Geotherm Res 260:127–145. https://doi.org/10.1016/j.jvolgeores.2013.04.018

Solaro C, Martel C, Champallier R, Boudon G, Balcone-Boissard H, Pichavant M (2019) Petrological and experimental constraints on magma storage for large pumiceous eruptions in Dominica island (Lesser Antilles). Bull Volcanol 81(9):55. https://doi.org/10.1007/s00445-019-1313-x

Sparks RSJ, Annen C, Blundy JD, Cashman KV, Rust AC, Jackson MD (2019) Formation and dynamics of magma reservoirs. Philos Trans A Math Phys Eng Sci 377(2139):20180019. https://doi.org/10.1098/rsta.2018.0019

Spear FS (1993) Metamorphic phase equilibria and pressure-temperature-time paths. Mineralogical Society of America, Washington, USA, 799 pp

Streck MJ (2008) Mineral Textures and Zoning as Evidence for Open System Processes. In: Putirka KD, and Tepley III FJ (ed) Minerals, Inclusions and Volcanic Processes, vol 69, Rev Mineral Geochem. Mineral Soc Am-Geochem Soc, pp 595–622

Sugawara T (2000) Thermodynamic analysis of Fe and Mg partitioning between plagioclase and silicate liquid. Contrib Mineral Petrol 138(2):101–113. https://doi.org/10.1007/s004100050011

Sugawara T (2001) Ferric iron partitioning between plagioclase and silicate liquid: thermodynamics and petrological applications. Contrib Mineral Petrol 141(6):659–686. https://doi.org/10.1007/s004100100267

Sun C, Graff M, Liang Y (2017) Trace element partitioning between plagioclase and silicate melt: the importance of temperature and plagioclase composition, with implications for terrestrial and lunar magmatism. Geochim Cosmochim Acta 206:273–295. https://doi.org/10.1016/j.gca.2017.03.003

Takagi D, Sato H, Nakagawa M (2005) Experimental study of a low-alkali tholeiite at 1–5 kbar: optimal condition for the crystallization of high-An plagioclase in hydrous arc tholeiite. Contrib Mineral Petrol 149(5):527–540. https://doi.org/10.1007/s00410-005-0666-7

Tepley FJ, Lundstrom CC, McDonough WF, Thompson A (2010) Trace element partitioning between high-An plagioclase and basaltic to basaltic andesite melt at 1 atmosphere pressure. Lithos 118(1–2):82–94. https://doi.org/10.1016/j.lithos.2010.04.001

Tomiya A, Takahashi E (2005) Evolution of the magma chamber beneath usu volcano since 1663: a natural laboratory for observing changing phenocryst compositions and textures. J Petrol 46(12):2395–2426. https://doi.org/10.1093/petrology/egi057

Tsuchiyama A (1985) Dissolution kinetics of plagioclase in the melt of the system diopside-albite-anorthite, and origin of dusty plagioclase in andesites. Contrib Mineral Petrol 89(1):1–16. https://doi.org/10.1007/BF01177585

Ubide Garralda T (2013) The Cretaceous alkaline magmatism in northeast Iberia: igneus processes and geodynamic implications. Departamento de Ciencias de la Tierra, Universidad de Zaragoza (España), PhD thesis, 248 pp

Ubide T, Galé C, Arranz E, Lago M, Larrea P (2014b) Clinopyroxene and amphibole crystal populations in a lamprophyre sill from the Catalonian Coastal Ranges (NE Spain): a record of magma history and a window to mineral-melt partitioning. Lithos 184–187:225–242. https://doi.org/10.1016/j.lithos.2013.10.029

Ubide T, Kamber BS (2018) Volcanic crystals as time capsules of eruption history. Nat Commun 9(1):326. https://doi.org/10.1038/s41467-017-02274-w

Ubide T, Wijbrans JR, Galé C, Arranz E, Lago M, Larrea P (2014a) Age of the Cretaceous alkaline magmatism in northeast Iberia: implications for the Alpine cycle in the Pyrenees. Tectonics 33(7):1444–1460. https://doi.org/10.1002/2013tc003511

Ustunisik G, Kilinc A, Nielsen RL (2014) New insights into the processes controlling compositional zoning in plagioclase. Lithos 200–201:80–93. https://doi.org/10.1016/j.lithos.2014.03.021

van Gerve TD, Neave DA, Almeev RR, Holtz F, Namur O (2020) Zoned crystal records of transcrustal magma transport, storage and differentiation: Insights from the shatsky rise oceanic plateau. J Petrol 61(8):egaa080. https://doi.org/10.1093/petrology/egaa080

Van Orman JA, Cherniak DJ, Kita NT (2014) Magnesium diffusion in plagioclase: Dependence on composition, and implications for thermal resetting of the 26Al–26Mg early solar system chronometer. Earth Planet Sci Lett 385:79–88. https://doi.org/10.1016/j.epsl.2013.10.026

Viccaro M, Giacomoni PP, Ferlito C, Cristofolini R (2010) Dynamics of magma supply at Mt. Etna volcano (Southern Italy) as revealed by textural and compositional features of plagioclase phenocrysts. Lithos 116(1–2):77–91. https://doi.org/10.1016/j.lithos.2009.12.012

Wallace PJ, Plank T, Edmonds M, Hauri EH (2015) Volatiles in Magmas. In: Sigurdsson H, Houghton B, McNutt S, Rymer H, and Stix J (ed) The Encyclopedia of Volcanoes (2nd Edition). Elsevier, pp 163–183

Watanabe K, Kitamura M (1992) Growth mechanisms of plagioclase in a basaltic melt. Mineral J 16(4):201–214. https://doi.org/10.2465/minerj.16.201

Waters LE, Lange RA (2015) An updated calibration of the plagioclase-liquid hygrometer-thermometer applicable to basalts through rhyolites. Am Mineral 100(10):2172–2184. https://doi.org/10.2138/am-2015-5232

Wieser PE, Kent AJR, Till CB, Abers GA (2023a) Geophysical and geochemical constraints on magma storage depths along the cascade arc: Knowns and unknowns. Geochem Geophys Geosyst 24:e2023GC011025. https://doi.org/10.1029/2023gc011025

Wieser PE, Kent AJR, Till CB, Donovan J, Neave DA, Blatter DL, Krawczynski MJ (2023b) Barometers behaving badly I: Assessing the influence of analytical and experimental uncertainty on clinopyroxene thermobarometry calculations at crustal conditions. J Petrol 64(2):1–27. https://doi.org/10.1093/petrology/egac126

Wilke M, Behrens H (1999) The dependence of the partitioning of iron and europium between plagioclase and hydrous tonalitic melt on oxygen fugacity. Contrib Mineral Petrol 137(1):102–114. https://doi.org/10.1007/s004100050585

Witt-Eickschen G, Seck HA, Mezger K, Eggins SM, Altherr R (2003) Lithospheric mantle evolution beneath the eifel (Germany): Constraints from Sr–Nd–Pb isotopes and trace element abundances in spinel peridotite and pyroxenite xenoliths. J Petrol 44(6):1077–1095. https://doi.org/10.1093/petrology/44.6.1077

Yagi K, Hariya Y, Onuma K, Fukushima N (1975) Stability relation of kaersutite. Journal of the Faculty of Science, Hokkaido University. Series 4. Geol Mineral 16(4):331–342